

Chapter 1

The Compact Muon Solenoid detector

The Compact Muon Solenoid (CMS) is housed at interaction point 5 of the LHC. The LHC is designed to pursue physics at the TeV scale. This is the scale where electroweak symmetry breaking is believed to occur [?]. While ~~this means that~~ the search for the standard model Higgs boson was the central driving design consideration, the wide range of possibilities for finding new physics signals requires a general purpose detector. ~~The expedient discovery of new physics through low cross section interactions requires high luminosity~~ CMS was optimized to make excellent measurements of muons. Muon capabilities developed for the Higgs boson can be used to study J/ψ . A versatile trigger is needed to accommodate the high interaction rates that accompany the high luminosities. By exploiting the versatility of the trigger and muon systems it is possible to explore processes like UPC J/ψ production, which push to the low energy edge of the experiment's capabilities.

~~The general purpose design of~~ CMS is dominated by the massive 4T superconducting solenoid at its core. The magnets is 13m long with a 6m diameter, and pushes the limits of power and compactness [?]. These two conflicting limits are achieved through the novel design of interweaving structural and conducting elements together in the coil of the solenoid.

Within the solenoid resides three different sub detectors. The inner most is the world's largest silicon tracker [?]. The tracker is surrounded by a highly effective lead tungstate crystal electromagnetic calorimeter (ECAL) [?]. ECAL is encapsulated in a brass scintillating hadronic calorime-

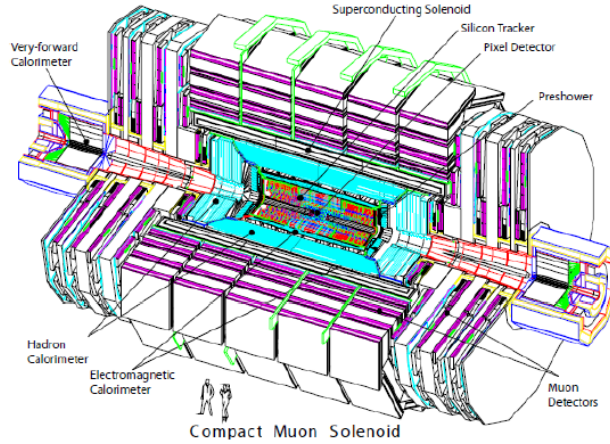


Figure 1.1: The Compact Muon Solenoid layout [?].

ter (HCAL). Outside the magnet, muon chambers are used to aid in the measurement and triggering of muon events. Altogether CMS weighs 12,500 metric tons, has a diameter of 14.6m, and a length of 21.6m [?].

1.1 Tracker

The Silicon Tracker [?] is the innermost sub-detector of CMS, and has active elements as close as 4.4cm to the interaction point [?]. The tracker has a length 5.8m, a diameter of 2.6m and covers a range in pseudorapidity of $|\eta| < 2.5$. At the center of the tracker are three rings of silicon pixels around the beam with two disks of silicon pixels to cap the rings. The pixel portion of the silicon tracker is comprised of 66×10^6 pixels. The silicon pixels are surrounded by silicon strips. The silicon strips are separated into 4 different sections: the Tracker Inner Barrel, the Tracker Inner Disk, the Tracker Outer Barrel, and the Tracker End Caps. The silicon strip detectors as a whole are comprised of 9.3×10^6 silicon strips. The high number of pixels and strips allow for the ability to distinguish and collect enough distinct points to reconstruct the path of the 1000 or so charged particles per bunch crossing expected at peak luminosity [?].

The amount of material present in the tracker is substantial enough to alter the path of particles as they pass through the tracker. Fig. 1.3 shows the amount of material in the tracker as a function

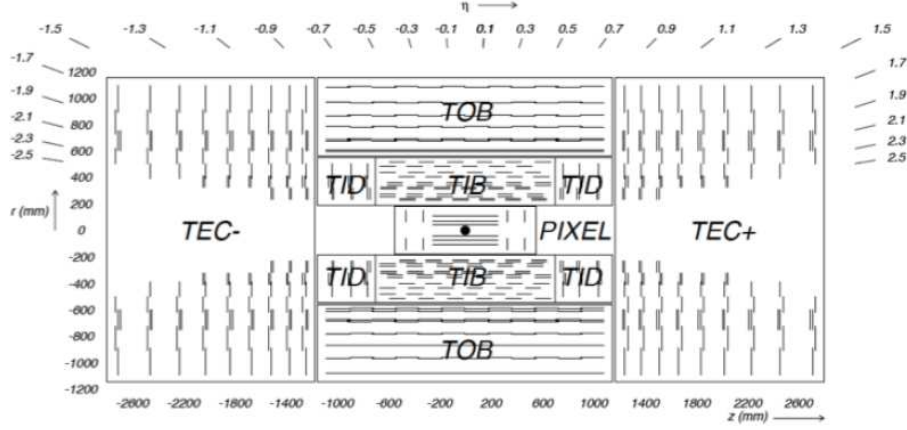


Figure 1.2: Layout of the silicon tracker with the pixels closest to the interaction point, marked with a black dot, and the strips segments beyond the pixels.

of radiation lengths (X_0). The λ radiation length is the mean distance a high-energy particle travels before giving up one e -fold of kinetic energy through electromagnetic interactions. For example, after one radiation length $E \rightarrow E/e$, where $e \sim 2.7$ the base of the natural logarithm. photon travels before interacting. As opposed to the deflection angle set by the strength of the magnetic field, the momentum resolution for lower momentum tracks is limited by the ~~lose~~ loss of energy due to multiple scattering of these particles off the material of the detector. For UPC J/ψ , this is the primary factor contributing to the resolution of the reconstructed muon tracks.

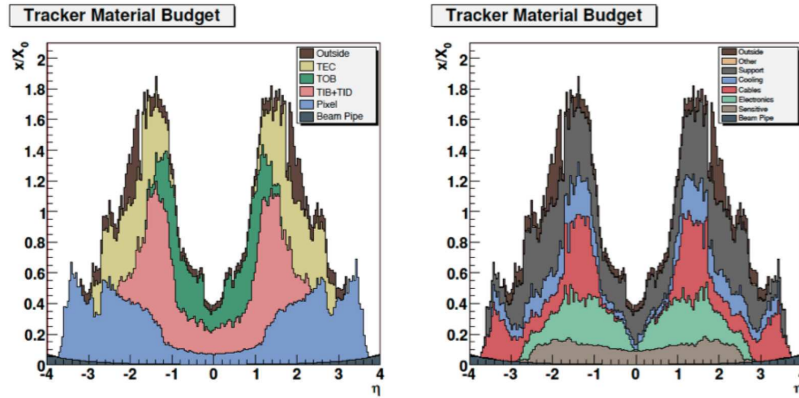


Figure 1.3: Material budget in the tracker broken down by sub-detector(left) and category (right) [?].

1.2 ECAL

The next detector beyond the tracker is the electromagnetic calorimeter system, ECAL. The calorimeter system is made of 61,200 lead tungstate (PbWO_4) crystals in the central barrel and 7,324 ~~on~~in each of the two endcaps [?]. The barrel (EB) covers a pseudorapidity range $|\eta| < 1.479$ and has an $\eta - \phi$ segmentation of approximately 0.0174×0.0174 , depending slightly on the position of the fixed sized crystals. Lead tungstate is very dense giving the ECAL crystals a high number of ~~interaction~~radiation lengths within a short depth. The crystals of the barrel have a depth of 230 mm corresponding to $25.8 X_0$. The endcaps (EE) cover the pseudorapidity region $1.479 < |\eta| < 3$. In the endcap the crystals have an exposed area of $28.62 \times 28.62 \text{ mm}^2$, and a depth of 220 mm corresponding to $24.7 X_0$. The energy resolution of the ECAL as measured by test beam data can be seen in Figure 1.4. The fractional energy resolution reduces quickly above 10 GeV and levels

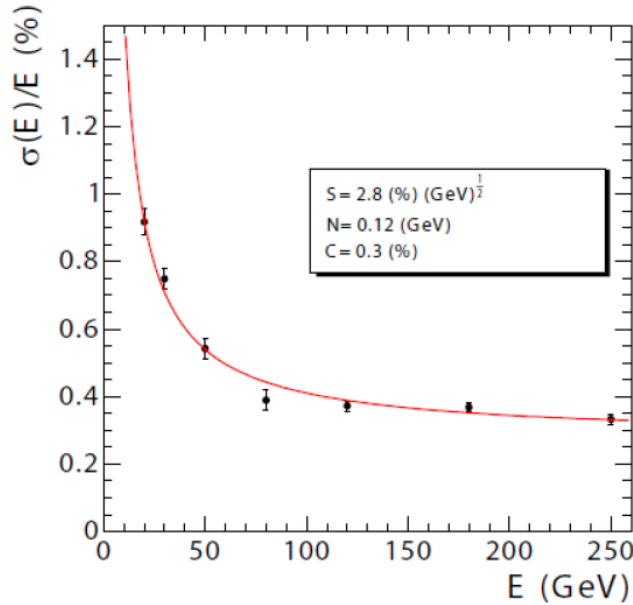


Figure 1.4: The energy resolution of ECAL as a function of energy [?].

off at about 0.5% for energies above 100 GeV. For J/ψ with rapidity near 2, the electron will carry ~~at least 10~~energies around 6 GeV and can be resolved by the ECAL.

1.3 HCAL

The HCAL [?] like the ECAL has both a barrel (HB) and endcaps (HE). The pseudorapidity region $|\eta| < 1.3$ is covered by HB [?]. HB has an $\eta - \phi$ segmentation of 0.0897×0.0897 , and is 25 times more sparsely granulated than EB. HE covers the pseudorapidity region $1.3 < |\eta| < 3$. HE, like EE and the tracker endcaps, is aligned ~~perpendicular~~ parallel to the beam axis resulting in granularity that changes with η . In the region $1.3 < |\eta| < 1.6$ HE has an $\eta - \phi$ segmentation of 0.0897×0.0897 . The $\eta - \phi$ ~~segmentation~~ cell size roughly doubles to 0.17×0.17 in the region $1.6 < |\eta| < 3$. The energy resolution of the barrel and endcaps can be seen in Figure 1.5. The thickness of the hadronic calorimeter is best described in interaction lengths, λ_I , which is the mean distance ~~for a particle to give up an e -fold of energy through nuclear interactions~~ a hadron travels before it experiences a nuclear interaction. At $\eta = 0$ the barrel has a thickness 5.82 interaction lengths (λ_I), and increases as the path length through the material increases to $10.6 \lambda_I$ at $|\eta| = 1.3$.

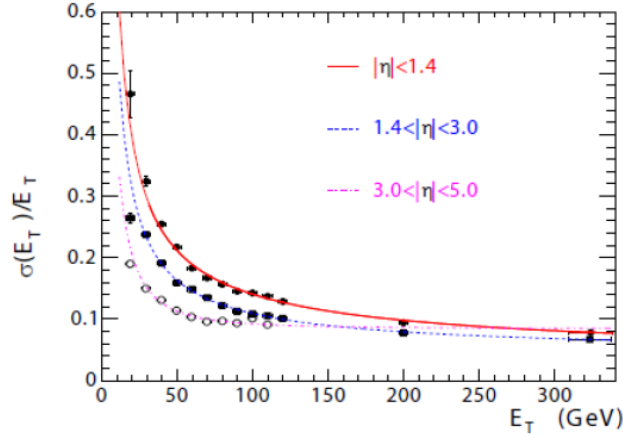


Figure 1.5: The E_T resolution of HCAL as a function of $|\eta|$ and E_T [?].

In addition to HB and HE, HCAL has two additional calorimeters. Because the space between ECAL and the magnet is restricted to 1.18 m, an outer hadronic calorimeter section (HO) is placed beyond the magnet in the region $|\eta| < 1.3$ [?]. The main function of HO is to collect energy from the highest energy hadrons before they reach the muon system. HO is not used in this analysis, but does contribute to the material budget. To increase the total calorimetric coverage, HCAL also

has a quartz fiber calorimeter (HF) in the forward region, $3 < |\eta| < 5$. For the majority of HF's 13 η rings the $\eta - \phi$ segmentation is 0.175×0.175 . In the lowest $|\eta|$ ring the segmentation is 0.111×0.175 in $\eta - \phi$. In the highest two $|\eta|$ rings the segmentation in ϕ is 0.349, with an η segmentation of 0.175 in the outer and 0.300 in the innermost ring. The longitudinal direction is effectively segmented by using both short and long fibers. The ~~energy deposited deeper than long~~ fibers are sensitive to energy deposited throughout the calorimeter, i.e. to both the hadronic and electromagnetic parts of the shower. The short fibers are only sensitive to the energy deposited more than 22cm ~~is measured in both the short and long fibers, where as the long fibers are present throughout inside the calorimeter, which is mainly hadronic.~~ This allows electromagnetic showers to be distinguished from purely hadronic showers [?].

The energy resolution for HF can be seen in Figure 1.5. As with the ECAL, the fractional resolution increases with energy. This is due to the random nature of shower development. At larger energies, the fluctuations in the shower of particles collected in the calorimeter tend to average out.

1.4 CASTOR

Very forward angles are covered at one end of CMS ($6.6 < \eta < 5.2$) by the CASTOR calorimeter [?]. CASTOR is 1.6m long and 0.6m in diameter and sits 14.4m away from the nominal interaction point. It is 1.6m long and 0.6m in diameter. CASTOR is a Cerenkov calorimeter made of quartz fibers/plates embedded in tungsten absorbers. The quartz and absorbers are inclined at 40° to the beam axis to maximize the amount of Cerenkov light. CASTOR is segmented into 16 ϕ -sectors and 14 z modules. The two front modules comprise the electromagnetic section of the calorimeter with a depth of 20 radiation lengths. Each of the electromagnetic channels has half the depth of the hadronic ones. The total thickness of CASTOR is about 10 interaction lengths.

1.5 ZDC

Beyond HF, the Zero Degree Calorimeters (ZDCs) [?] covers the very forward rapidity region. The ZDCs sit between the beam pipes on either side of the interaction point covering the area around $\theta = 0, |\eta| > 8.3$. In heavy ion collisions the ZDC has the ability to measure neutral particles that do not participate in the collision [?]. This detector plays an important role in the analysis described in this thesis by measuring energy due to neutrons produced by photon-induced nuclear break. These measurements are used to identify events with asymmetric neutron emission, reducing the contribution to the sample by peripheral heavy-ion

The ZDC has a total of 18 channels. Half of these 18 channels are on either side of the interaction point. The 9 channels on the side of CMS that correspond to positive η are denoted ZDC^+ , where as the 9 channels on the negative side are denoted ZDC^- . The 9 channels on each side are further sub-divided into an electro-magnetic (EM) section and a hadronic (HAD) section. The EM section is positioned in front of the HAD section with respect to the interaction point and is segmented transverse to the beam direction. The 5 EM sections are positioned in front to absorb the energy from electro-magnetically induced showers, which develop over a shorter distance than hadronically induced showers. The transverse segmentation allows for a measurement of the transverse shower width and the size of the beam spot at the ZDC. The HAD section is segmented in the direction of the beam and consists of 4 channels. The longitudinal segmentation allows for absorption of the full extended hadronic shower and the ability to measure the longitudinal shower shape.

Each of the 18 channels contains a tungsten target and quartz fibers. The dense tungsten target is used to initiate the shower. The quartz fibers shine Cerenkov light as the high momentum charged particles from the shower pass through it. the light from the quartz fibers is channeled to photo-multiplier tubes, one for each ZDC channel. Through a cascade of photon induced electrical discharges, the photo-multiplier converts the Cerenkov light to an electrical pulse.

This electrical pulse travels ~ 200 m down a coaxial cable from the LHC tunnel to the counting house in the CMS service cavern. There the electrical pulse is digitized by the Charge Integrator

and Encoder (QIE). The QIE integrates the current each 25 ns. The charge is then mapped logarithmically to the 128 bits. This bit is sent across a small fiber optic cable to the HTR firmware card. Here each 25 ns signal is stored in a 250 ns buffer, and the timing is synchronized with the rest of the detector to ensure the ZDC signal arrives at the central data acquisition system at the same time as the other sub detectors from the same collision.

1.6 Muons

The muon system [?] resides just outside of the superconducting magnet. It consists of three complementary systems: drift tube (DT) chambers in the barrel, cathode strip chambers (CSC) in the endcaps, and resistive plate chambers (RPC) in both the barrel and endcap regions [?]. Each of these gaseous detectors function in the same way. As the muon penetrates the gas volume electrons are knocked off of the gas atoms and these electrons are collected in the positively charged anode, whereas the ionized gas moves to the cathode. The DTs in the barrel and the CSCs in the endcap have better spatial precision relative to the RPCs, which are quicker and have more precise timing. The combination of the DTs and RPCs in the barrel and the CSCs and RPCs in the endcap allow for fast triggering and muon identification during data reconstruction.

As seen in Fig. 1.6, the DTs reside only in the barrel, covering the region $|\eta| < 1.2$. Consisting of a total of 172,000 cells, the DT cells are collected into 250 chambers. The DT chambers are interwoven into the magnet field return yoke and are labeled by 5 segmentations in z , YB-2 to YB+2. Each z segment is divided into 12 ϕ segments labeled 1 at $\phi = 0$ and going to 12 rotating in positive ϕ with segments 4 and 10 containing 2 chambers. The segmentation in r is divided into four parts, MB1-MB4. Fig. 1.7 shows how each chamber is made of three super layers. Super layers $SL \Phi_1$ and $SL \Phi_2$ measure (r, ϕ) , whereas $SL \Theta$ measures z .

The RPCs complement the DTs in the barrel and the CSCs in the endcap primarily for the purpose of triggering. Throughout the barrel and endcap there are a total of 1020 RPC modules, 480 in the barrel and 540 in the endcap. Denoted by the red lines in Fig. 1.6, the RPCs are

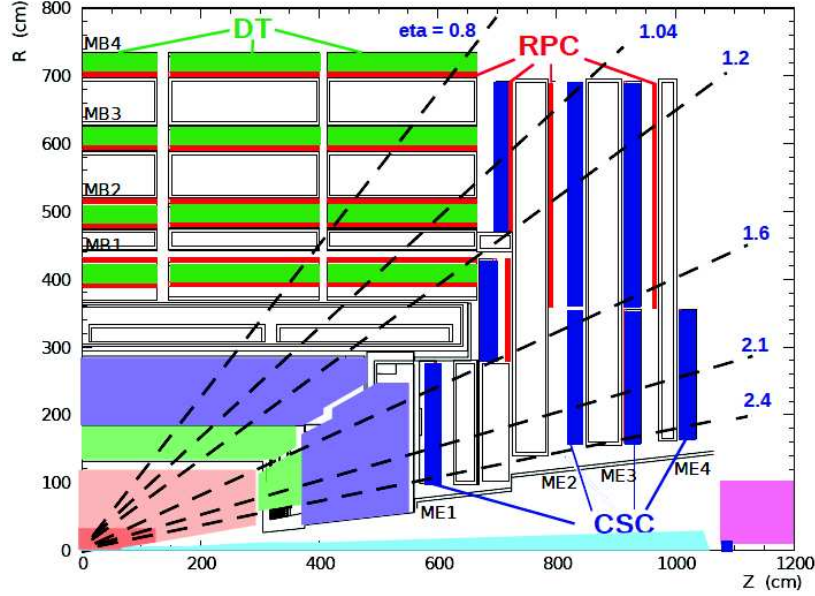


Figure 1.6: The CMS muon system showing the four DT stations in the barrel (MB1-MB4), the four CSC stations in the endcap (ME1-ME4), and the RPC stations.

mounted on both sides of the DTs in the barrel for the inner most layers, MB1 and MB2. For the outer two layers of the barrel, MB3 and MB4, a single layer of RPCs is mounted on the inner side of the DTs. Each corresponding DT segment has two RPCs modules, except in MB2 where some segments contain 3 RPC modules. The outer ring of the muon endcap are instrumented with RPCs covering up to $|\eta| = 1.6$.

There are a total of 468 CSC modules in the muon system endcap. For the sectors in z , ME2, ME3, and ME4 in the endcap, the modules in the ring closest to the beam are covering 20° in ϕ . The modules in ME1 and the modules in beyond the inner ring in ME2 and ME3 have a $10^\circ \phi$ segmentation. The 2 million wires of the CSCs are grouped into 400,000 channels and are powered with 9000 high voltage supplies. The resolution of the CSCs is on the order of 1mm for position measurements in the plane perpendicular to the beam and they are 99% efficient for muons that pass through all four sectors, ME1, ME2, ME3, and ME4. Because of the relatively low momentum of the muons originating from J/ψ in UPC events, the muons in the analysis discussed in this thesis are all in the range $1.6 < |\eta| < 2.4$ and rely on the CSCs for triggering.

The primary function of the muon systems are to allow for triggering on and identification

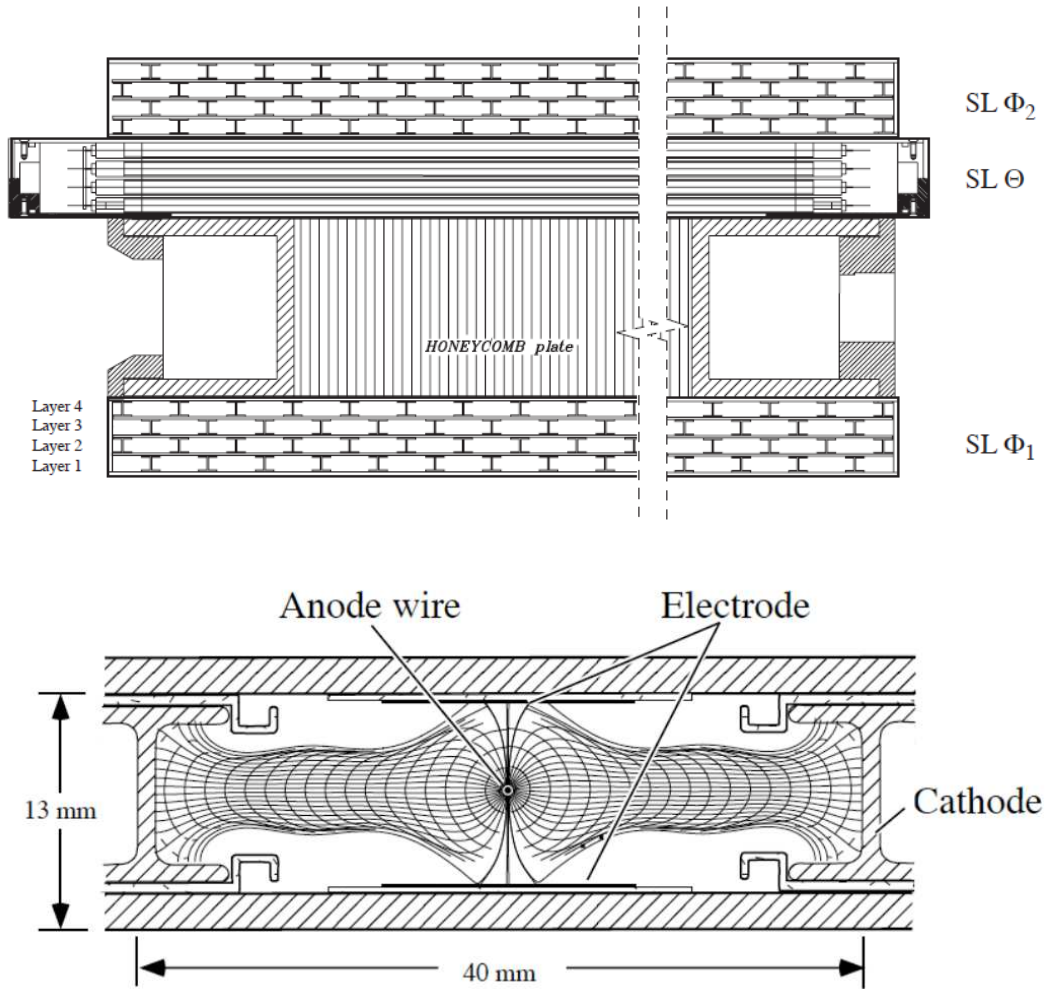


Figure 1.7: Schematic of the DT chambers and an individual DT cell.

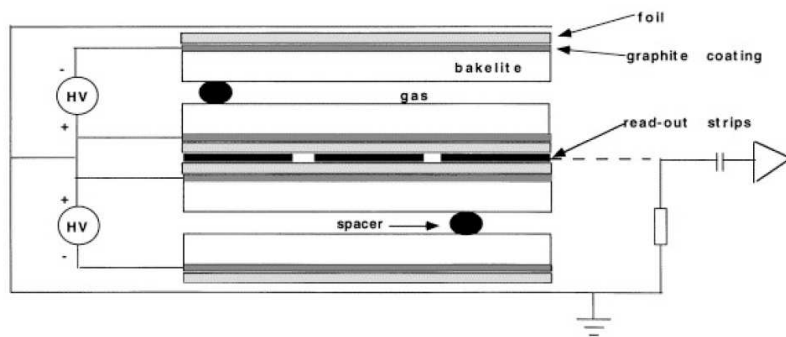


Figure 1.8: Schematic of a RPC cell.

164 of is to trigger on and identify muons. The tracker is still the primary instrument for measuring
 165 the muons. Fig. 1.10 shows the resolution of reconstructed muons with the tracker only is only

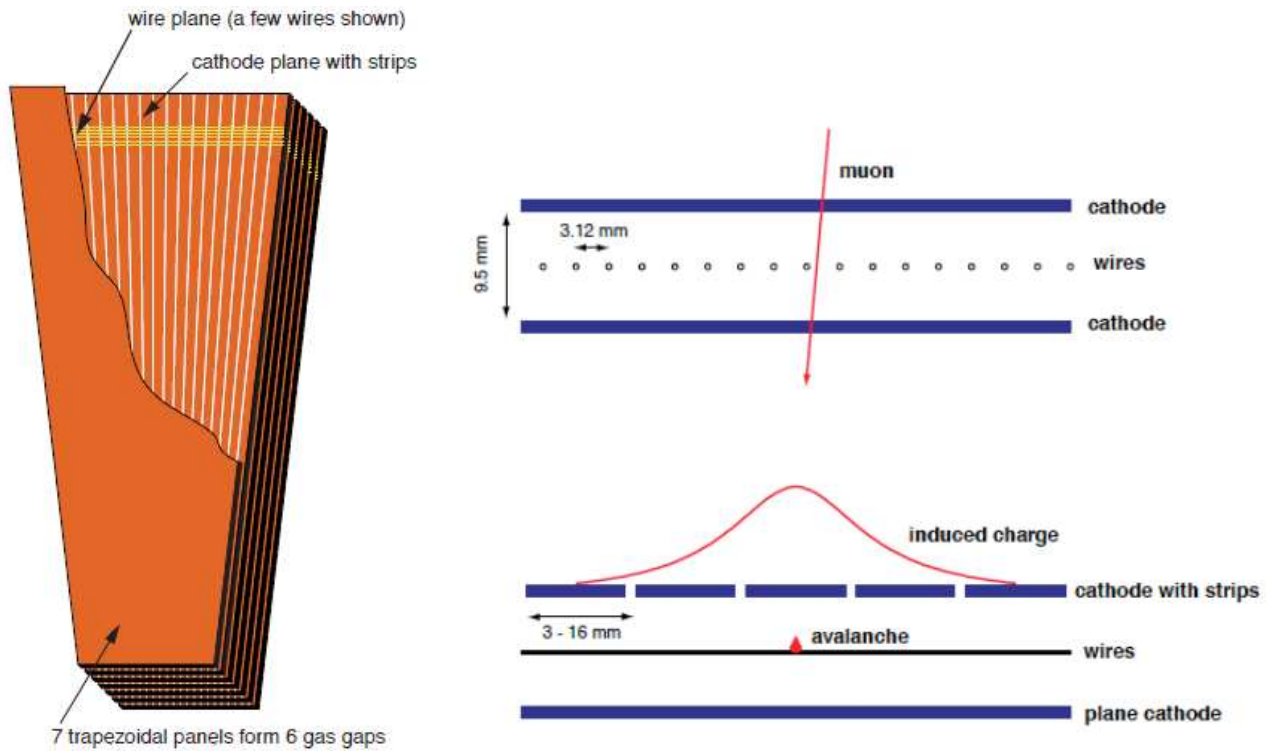


Figure 1.9: Schematic of the CSC chambers and an individual CSC cell.

~~improved upon~~ that the muon system only improves the momentum resolution for muons with momenta above 100 GeV. For UPC J/ψ events, where muons momenta are between ~~1-2~~ 4-8 GeV, the muon system does not provide any advantage in terms of improved resolution. The muon system is however important in ~~distiguishing~~ distinguishing which tracks are due to muons as opposed to other charged particles. Because of their ~~increase~~ much larger mass relative to electrons, muons emit less bremsstrahlung, or braking radiation, as ~~it penetrates~~ they penetrate the inner layers of the CMS on its way to the muon systems. Fig. 1.11 shows the amount of material traversed by particles traveling through CMS as a function of $|\eta|$. The total of nearly 10 interaction lengths between the interaction point and the muon chambers ensures that hadrons like charged pions, which ~~nearly~~ almost exclusively decay to muons, are ~~collected~~ absorbed in the calorimeters before converting to muons. By eliminating backgrounds from both electrons and hadrons, the CMS muons system allows for identification of muons for both triggering and reconstruction.

The low-momentum nature of UPC physics creates complications due to the large amount of

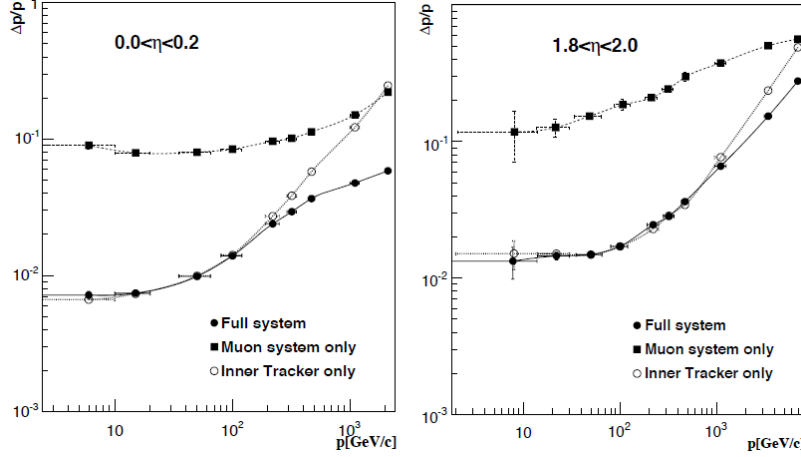


Figure 1.10: The momentum resolution for muons using only the tracker and the whole muon system in the barrel (left) and end cap (right) [?].

material between the interaction point and the muon systems. About 3 GeV of momentum is needed to reach the first layers of the muon system. In the rest frame of the J/ψ , the J/ψ equally shares its rest mass with its decay products creating 2 muons with momenta of about 1.5 GeV. For these daughter muons to reach the muon system, their parent J/ψ must be pushed to higher momentum by the initial particles which created the J/ψ . For this reason, muons from UPC J/ψ s are only detected at higher η values. Understanding this momentum restriction of the muon system was a major focus of the analysis discussed in this thesis with details described in Section. 4.4.

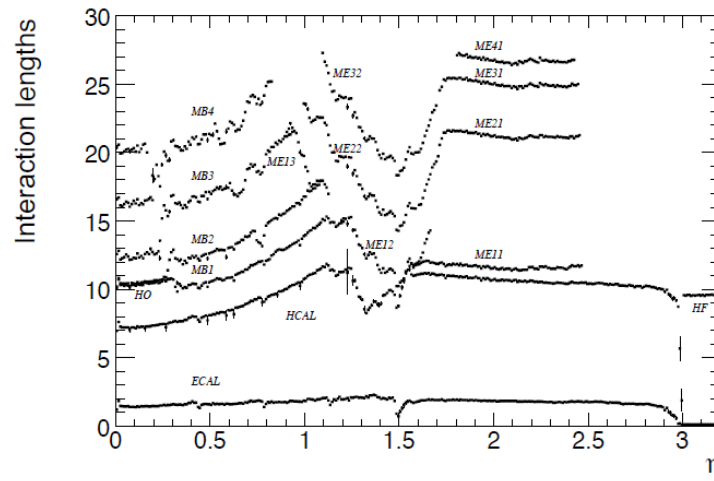


Figure 1.11: The amount of material in CMS as a function of η in number of interaction lengths [?].

1.7 Trigger

The CMS trigger is two tiered [?, ?]. The L1 trigger is the lower level hardware based system. The High Level Trigger (HLT) is a software base and runs on a computer farm located at point 5.

The purpose of the L1 trigger is to make quick decisions about which events will be kept temporarily for further processing. ~~The L1 trigger~~ It uses only information from the calorimeter and muon systems and is used to identify events where the tracker should be read out. ~~Only the calorimeters and the muon system are used in the L1 trigger. Each of the sub-detectors has its triggering hardware.~~ The output from the sub-detectors is synchronized to ensure that the signal from each of the sub-detectors comes from the same collision. ~~The global trigger hardware then makes the final decision to initiate the HLT and to read out the tracker.~~

If an event passes the L1 trigger, the data from all the sub-detectors, including the tracker are sent to the HLT computing farm. At this level the raw data from all the sub-detectors is unpacked and combined. The information from the calorimeters, muon system, and tracker can all be used to reconstruct basic physic objects in the HLT farm. For example, tracks can be associated with either ECAL energy clusters to form electron candidates, or tracks can be combined with hits in the muon system to create muon candidates. At the HLT, the whole detector is used to select events. The raw data from the events that survive the HLT are recorded permanently, those that do not are lost forever.

The HLT farm must always be ready to accept events from the L1 trigger. For this reason, the amount of computing time each HLT trigger path uses must be balanced. For more rare L1 triggers, which will occur at a lower rate, more complex reconstruction software can be used. Conversely, simpler, faster, methods must be used for more common high rate triggers. Because of this time constraint in the HLT farm, the reconstruction algorithms used for triggering tended to differ from the final reconstruction algorithms. In the HLT these algorithms are optimized for quickness, whereas the final reconstruction is optimized for precision and accuracy. By having the ability to spend different amounts of computing time on different L1 triggered events, the complexity of the event selection offered by the HLT is heightened.

213 The two tiered triggering system creates very low dead times while maintaining purity and
214 selectivity. ~~During data taking the L1 trigger is continuously monitoring, and the HLT allows for~~
215 ~~sophisticated event selection.~~ The wide gamete of physics topics that are pursued by the CMS
216 collaboration are a testament to the effectiveness and versatility of the CMS two tiered triggering
217 system. In Chapter 3, the development of L1 triggers and HLT paths for selecting UPC evens is
218 discussed.

Chapter 2

ZDC reconstruction

2.1 Nuclear break-up determination

As described in Section ??, UPC J/ψ photoproduction can be accompanied by the emission of neutrons from either of the two colliding nuclei. The various neutron emission scenarios, or break-up modes, can be distinguished by the two ZDCs. By separating events where the ZDC signal is consistent with 1 neutron versus several neutrons, or where neutrons are present on only one or both sides, the fraction of events which corresponds to a given break-up mode can be measured and compared to theory.

In order to maximize the ability to explore the one neutron peak, which sits at the bottom of the ZDCs dynamic range, a new ZDC reconstruction method was devised. This new reconstruction method was then used to establish ~~a one neutron and many neutron threshold~~thresholds for one and more than one neutron in each ZDC. This section describes the ZDC signal reconstruction and how the neutron thresholds on this signal were set.

2.1.1 ZDC signal reconstruction

The signal from each ZDC is built up from the pulse shapes for each of the 18 individual ZDC channels. The pulse shape is recorded in 250 ns second chunks and is divided into 10 time slices

of 25 ns (see Fig 2.1). Counting from 0, the 4th time slice is synced with the timing of the rest of the detector and corresponds to when the products of the recorded collision reached the ZDC. The **channel**-signal is therefore taken from the 4th time slice.

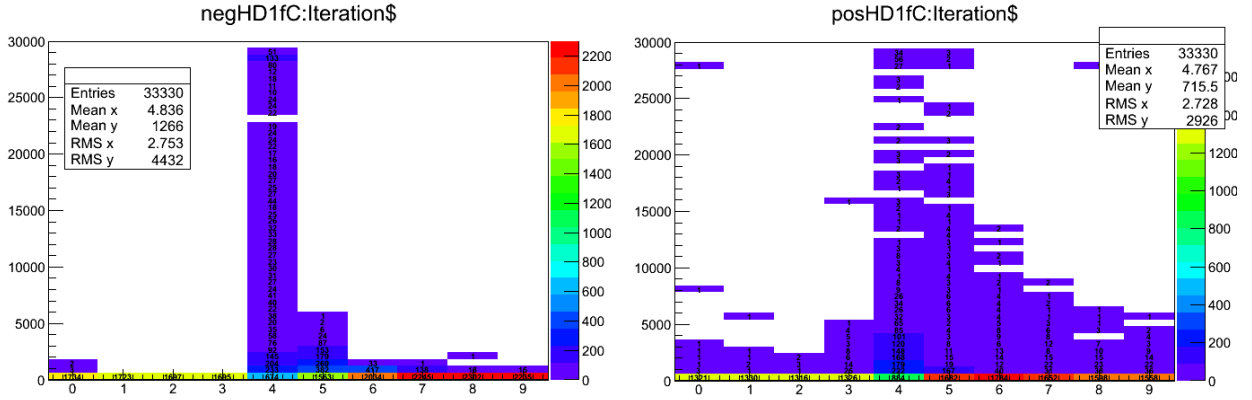


Figure 2.1: Average ZDC pluse shape is plotted as the charge as a function of time slice for the first hadronic from ZDC^- (left) and ZDC^+ (right).

The ZDC signal sits on top of a low frequency noise pedestal with a period of about 2μ seconds. Over the time scale of 250 ns, this low frequency noise signal appears as a constant that shifts randomly from event to event. The contribution from this noise is therefore measured event by event in order to subtract it. Time slice 5 is used for this purpose. Time slices 1 and 2 could also be used to estimate the low frequency noise. However because the noise fluctuates to negative values of charge that cannot be measured, these time slices can only provide a measurement of the noise half the time. By using time slice 5 which contains the falling tail of the signal, the noise can be measured any time the signal raises significantly above the noise. If the fraction of signal in time slice 4 and 5 are constant and the noise contributes the same value to both time slices, the following formula is applicable:

$$Ts4 \propto (Ts4 + C) - (Ts5 + C) = Ts4 - R_{Ts5/Ts4} Ts4 = Ts4(1 - R_{Ts5/Ts4}), \quad (2.1)$$

where $Ts4$ is the signal contribution in time slice 4, $Ts5$ is the signal contribution to time slice 5, C is a random noise constant from the low frequency noise, and $R_{Ts5/Ts4}$ is the ratio between the

signal contribution from time slice 5 over time slice 4. Figure 2.2 demonstrates the consistency of the fraction and validates the unconventional method of using the falling tail of the signal to estimate the low frequency noise. By using time slice 5, the chances of measuring the noise are maximized. Separating the signal from the noise is especially important because the ZDC signal for the one neutron peak sits near the noise at the bottom of the ZDC dynamic range.

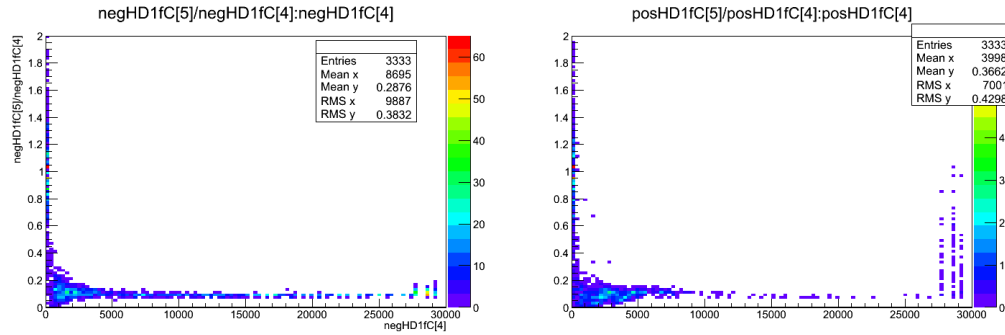


Figure 2.2: The fraction of signal in time slice 5 over time slice 4 as a function of the signal in time slice 5 in ZDC⁻ (left) and ZDC⁺ (right).

When summing the 9 channels in each ZDC only channels with signals above zero in time slices 4 and 5 were included. The EM, electromagnetic, section of the calorimeter is more densely packed with quartz fibers and therefore has a higher gain relative to the HAD, hadronic, section. To account for this, the EM channels were weighted with a factor of 0.1 to match the HAD channel gains.

2.1.2 Determination of the one neutron thresholds

The ZDC thresholds used to establish the various break-up modes were measured from zero bias data. Figure 2.3 shows the weighted sum of the EM and HAD sections for ZDC⁻ and ZDC⁺ for the zero bias dataset. The neutron spectrum for this dataset is not biased since the trigger only required that both beams were present in CMS. This dataset does, however, include a significant electronic noise contribution due to events where no neutrons are emitted in the direction of the ZDC. It is clear from Fig. 2.3 that the gain of ZDC⁺ is lower than that of ZDC⁻. This is because of a damaged phototube on the first HAD section of ZDC⁺.

To determine the thresholds for one and multiple neutrons, the ZDC^+ and ZDC^- spectra were fit. ~~Four Gaussian functions were combined to fit the spectra~~ each fit to the sum of four Gaussians. The electronic noise was fit to a Gaussian around zero. The one, two, and three neutron peaks are fit to Gaussians that are successively broader. The mean of each peak was initially set to multiples of the mean of the one neutron peak. The threshold for a neutron in the ZDC was taken from the

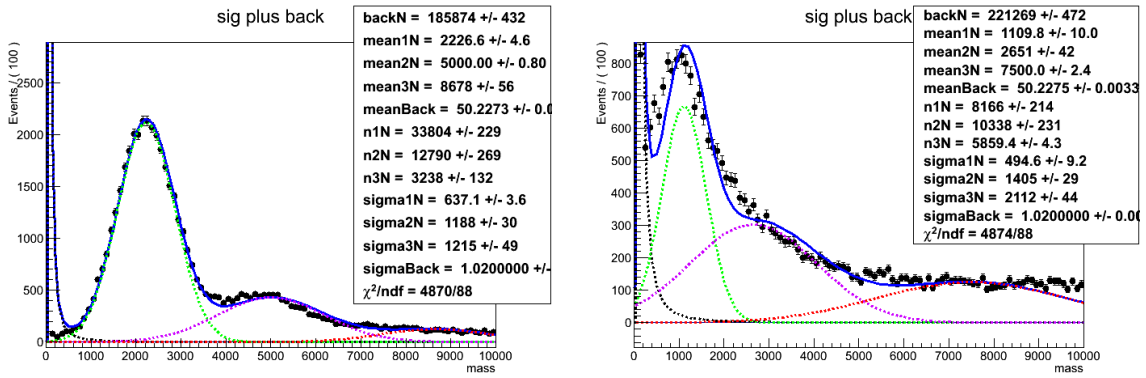


Figure 2.3: Fit to the signal spectra for ZDC^- (left) and ZDC^+ (right)

fits in Fig. 2.3. Any signal greater 2σ below the mean of the one neutron peak was considered signal. Any signal greater than 2σ above was considered multiple neutrons. The single neutron break up modes were separated from the multiple neutron modes by use of these definitions.

Several of the break-up mode calculations that have been done involve single sided configurations where neutrons are present on one side of the interaction point and not the other. These modes can be hard to identify because the single neutron peak in ZDC^+ overlaps with the noise peak at zero. To identify events where the ZDCs only measured noise, the noise ~~spectrum~~ spectra were measured directly. Placing an additional criteria based on the ZDCs noise distributions for when the ZDCs are devoid of signal provides assurance that the events tagged as single sided events are truly single sided.

The noise distributions for the EM sections and the HAD sections were measured separately from out of time time slices. In Fig. 2.1 higher than average signal can be seen in the 0th time slice, which precedes the main signal time slice time slice 4 by 200 ns. This is due to events where activity was present in the ZDC for two consecutive collisions. Time slices 1 and 2, however,

288 occurred between collisions. These time slices, which occur out of time, were used to measure the
noise spectrum.

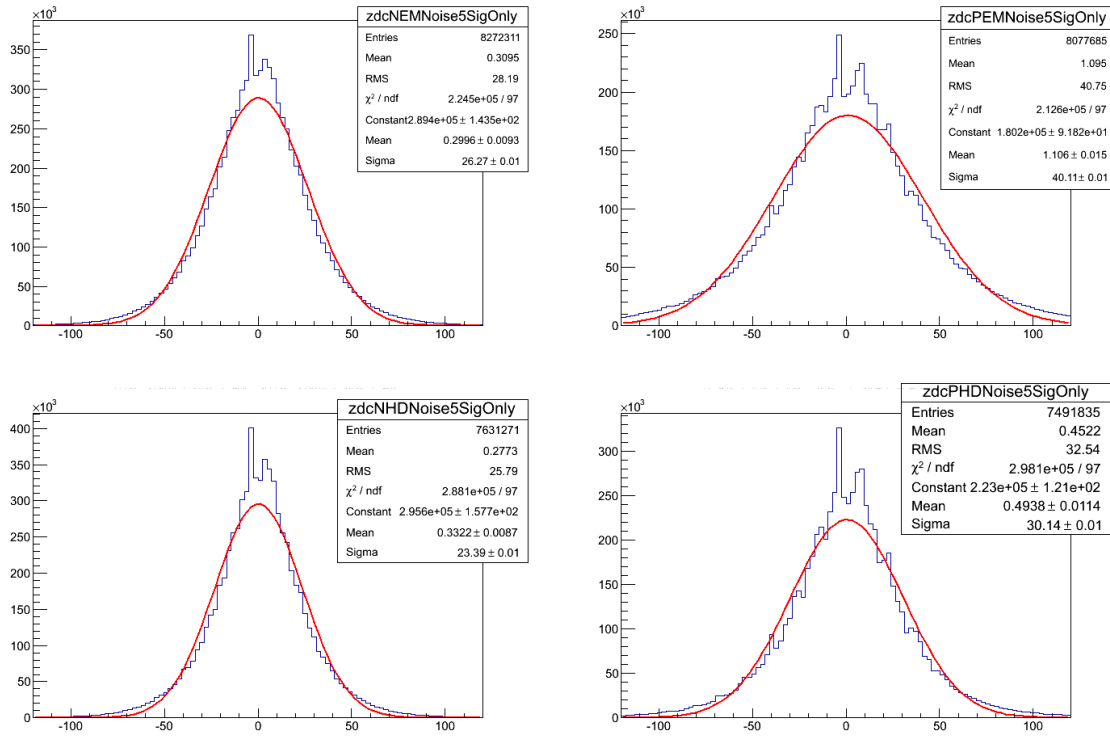


Figure 2.4: ZDC noise spectra from ZDC⁻ EM section (upper left), ZDC⁺ EM section (upper right), ZDC⁻ HAD section (lower left), and ZDC⁺ HAD section (lower right) from out of time slices.

289

290 As with the signal measurements, the low frequency noise pedestal is subtracted event by
291 event by subtracting time slice 2 from time slice 1 leaving only the high frequency noise. The
292 noise distributions do not depend on the amount of quartz fibers, but because the signal does, the
293 noise distributions for EM and HAD sections are measured separately. Figure 2.4 shows the noise
294 spectrum for each of the EM and HAD sections for the two ZDCs. If the HAD or EM signals
295 measured from time slices which match the timing for a collision, time slices 4 and 5, are less than
296 2σ above the mean of the noise distribution or lower, these sections are considered consistent with
297 noise. A ZDC is considered consistent with noise if both the HAD section and EM section from
298 that ZDC have signal measurements consistent with noise.

2.1.3 ZDC reconstruction method comparison

In this section the nominal ZDC reconstruction method designed for this thesis is compared to an alternative ~~comparison~~ method. This additional method, used in previous ZDC measurements, differs in the way the signal time slices are used to calculate the signal from each channel. In the additional ~~comparison~~ alternative method, the signal is taken from the sum of time slices 4, 5, and 6. To estimate the event by event noise pedestal the sum of time slice 1 and 2 are used. The signal for an individual ZDC channel is then calculated as the sum of the signal time slices minus the sum of the noise time slices weighted by a factor of 3/2 to account for the differing number of noise versus signal time slices. As in the nominal method described in Section 2.1, the ~~comparison~~ alternative method combines the channels to create a signal measurement from the whole of each side of the ZDC, one measurement for ZDC^+ , and one for ZDC^- . The noise subtracted signal from each of the HAD channels are added together. Then the EM section channels are summed. The EM section is weighted by a factor of 0.1 as in the nominal method. After the weighting the EM and HAD channels are added to each to create one measurement for ZDC^+ and another measurement for ZDC^- . Figure 2.5 shows the spectra for ZDC^+ and ZDC^- using the ~~comparison~~ alternative method. The same fit used for the nominal method is applied to the ~~comparison~~ alternative method. As in the nominal method, the single neutron threshold is set to 2σ below the mean from the fit to the one neutron peak. The multi-neutron threshold was set to 2σ above the one neutron peak.

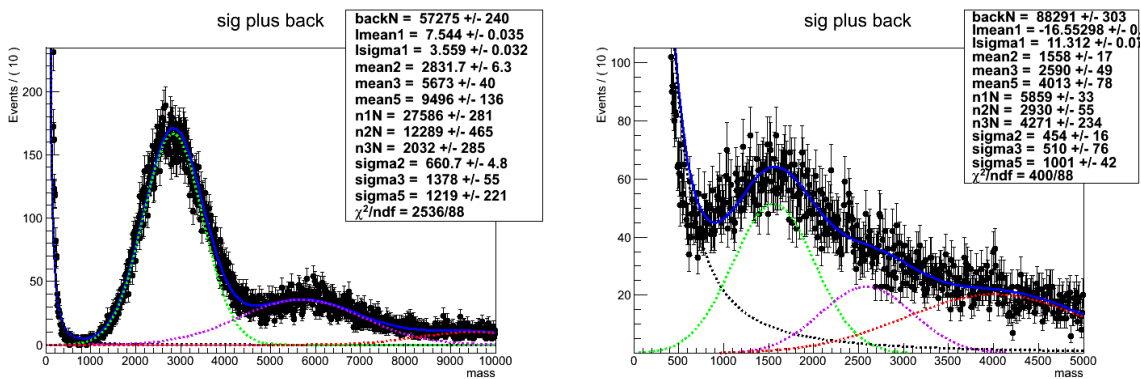


Figure 2.5: Fit to charge spectrum from ZDC^- (left) and ZDC^+ (right) using the ~~comparison~~ alternative reconstruction method

The advantage of the ~~comparison~~alternative method is that by using multiple signal and noise time slices the signal and noise are effectively averaged reducing time slice to time slice fluctuations. However, by using time slices 1 and 2 for measuring the noise, the noise can only be measured half the time due to unmeasurable negative fluctuations of the dominant low frequency component of the noise. The nominal method relative to the ~~comparison~~alternative method separates low signal from the noise more effectively for both sides of the ZDC. This is particularly important for ZDC^+ where the 1st HAD section had a lower gain than the other sections. The ZDC^+ and ZDC^- signals near the one neutron peak using the ~~comparison~~alternative and nominal reconstruction methods were plotted for comparison in Fig. 2.6. In Fig. 2.6, the shrinking of width

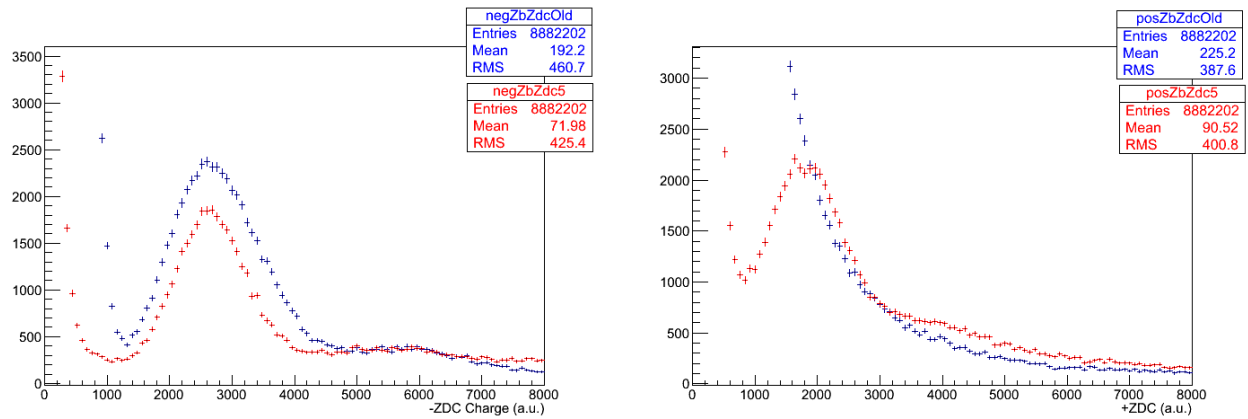


Figure 2.6: Comparison of the nominal (red) ZDC reconstruction method and the ~~comparison~~alternative (blue) method for ZDC^- (left) and ZDC^+ (right).

of the noise peak around zero in the nominal method versus the old method is apparent for both ZDC^+ and ZDC^- . For the ~~comparison~~alternative method no single neutron peak is resolved in ZDC^+ , whereas the single neutron peak is resolved using the nominal method.

Timing cuts were applied to enhance the signal relative to the background in order to resolve the one neutron peak in ZDC^+ using the ~~comparison~~alternative method. Because the products of the collision are synced with time slice 4, noise can be rejected by selecting channels where the maximum signal falls into time slice 4. The noise will have no preferred time slice (see Fig. 2.1). Using this fact, ~~signal can be preferably~~neutron events can be selected by requiring that the hadronic channels of the ZDC have a peak signal in the fourth time slice. Through these timing cuts the

single neutron peak was recovered using the ~~comparison~~-alternative reconstruction for ZDC^+ .

To examine the effectiveness of the timing cuts, event by event noise subtraction was removed from the ~~comparison~~-alternative reconstruction. The signal from each channel was taken from time slices 4,5, and 6 with out subtracting 1 and 2. The signal spectrum from ZDC^- was then plotted with the result shown in Fig. 2.7. As each additional hadronic channel is required to have a

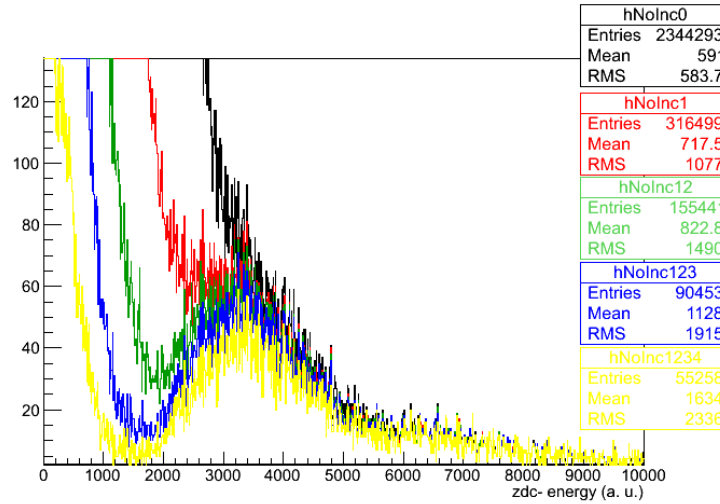


Figure 2.7: Effects of requiring in-time signal in successively more ZDC^- hadronic channels, no timing, at least one (red), at least two (green), at least three (blue), and all four (yellow) HAD channels have a maximum signal in the fourth time slice.

maximum signal in the fourth time slice, the single neutron peak emerges. Figure 2.7 demonstrates that the single neutron peak can be recovered from the noise using timing cuts alone.

Using the ~~comparison~~-alternative noise subtraction method, the same signal that emerges from the timing cuts alone appear without timing cuts. Figure 2.8 confirms that both noise subtraction and the timing requirement produce the same signal. This gives confidence that the signal is not an artifact of either cut, but the true neutron signal.

Figure 2.8 and Fig. 2.7 demonstrate the consistency of using timing cuts and noise subtraction to enhance the signal neutron peak. Figure 2.8 confirms the legitimacy of the timing requirement method in ZDC^- by showing that the same signal emerges from the noise subtraction method as the timing method. Fig. 2.6 demonstrates the correspondence between the nominal noise subtraction method and the ~~comparison~~-alternative method in ZDC^- where the signal is better separated from

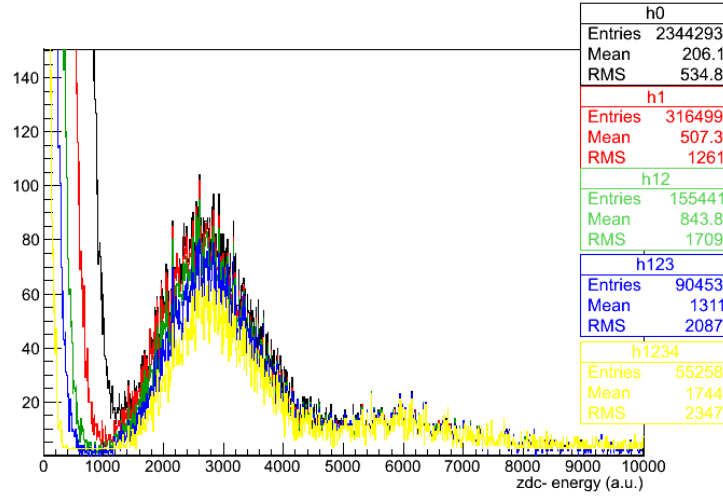


Figure 2.8: Effect of ZDC signal timing requirements after noise subtraction.

the electronic noise. This provides confidence that the signal seen in ZDC^+ using the nominal
method is the one neutron peak.

Chapter 3

UPC trigger development for CMS

Rare physics process at the LHC require dedicated triggers in order to sort these processes from the billions of ordinary nucleus-nucleus collisions. Unlike most heavy-ion triggers, UPC triggers are optimized for low- p_T and low multiplicity events. For this reason trigger development specific to UPC events was required to carry out the analysis in this thesis.

The increase in collision rate of the LHC PbPb beams from 2010 to 2011 was nearly a factor of 15. To accommodate this increase in rate, the 2011 trigger scheme needed to be more selective than in 2010 where CMS could take any event which appeared to have a collision. The available bandwidth was allocated equally amongst the various heavy ion analysis groups to pursue as wide a physics program as possible. From this consideration, bandwidth limits were placed on the trigger rates for each analysis group's trigger package.

3.1 L1 trigger

The UPC L1 triggers were designed to study UPC J/ψ production via the dimuon and dielectron channels (see Section 1.7). To achieve this, the loosest muon and electron triggers were combined with a trigger on energy in the ZDCs and no activity in BSCs (BSC veto). Additional triggers were commissioned in case radiation damage during the run reduced the sensitivity of the BSCs. This required no activity in HF (HF veto). These triggers are summarized in Table 3.1. The ECAL2

and ECAL5 triggers in Table 3.1 indicate a ~~5-and-2~~ and 5 GeV threshold on E_T measured in the ECAL. The MuonOpen trigger indicates that the trigger only requires a muon candidate in one of the three muon sub-systems and that there is no momentum threshold. ZDC in the trigger names indicate energy constant with at least one neutron. The sign on the ZDC label indicates which of the two ZDCs is required.

L1 trigger name	Rate (Hz)	Prescale	Id	Type
MuonOpen and (ZDC ⁺ or ZDC ⁻) and BSC veto	2.1	1	1	Physics
ECAL2 and (ZDC ⁺ or ZDC ⁻) and BSC veto	1.8	2	2	
ECAL5 and (ZDC ⁺ or ZDC ⁻) and BSC veto	0.3	1	3	
(ZDC ⁺ or ZDC ⁻)	35	1500	4	Monitor
MuonOpen and (ZDC ⁺ or ZDC ⁻) and HF veto	0	off	5	Backup
ECAL2 and (ZDC ⁺ or ZDC ⁻) and HF veto	0	off	6	
ECAL5 and (ZDC ⁺ or ZDC ⁻) and HF veto	0	off	7	

Table 3.1: List of 2011 L1 seeds.

The cumulative L1 trigger rate for all the UPC L1 trigger seeds was required to be no greater than 200 Hz. This requirement ~~comes~~ came from the need to keep the tracker read-out rate low. The trackers baseline voltage can fluctuate due to the high tracker hit multiplicities in PbPb collisions. In order to monitor the zero suppression of the tracker, the zero suppression algorithm was executed using the HLT computing farm rather than in the tracker firmware.

~~In order to record the efficiency monitoring data, the ZDC triggers were reduce to a lower rate by only keeping a fraction of the total trigger rate~~ The (ZDC⁺ or ZDC⁻) was used to estimate the efficiency of the UPC electron and muon triggers. The factor that the ~~trigger~~ rate is reduced by is called the prescale. A prescale of 2 for example means that half the triggers that were accepted. If the prescale is set to 1, then whole trigger rate is accepted. The prescale factors for the triggers were set to balance the competing objectives of rate reduction and increasing the overlap between the monitoring and signal triggers.

3.2 HLT trigger

An event must pass the selection criteria of an HLT path in order to be recorded. As opposed to the L1 trigger, which has access only to information from calorimeters and muon chambers, the HLT has access to all of the CMS sub-detectors including the tracker. Reconstruction of a track in the pixel detector is used by the UPC trigger paths. The use of the pixel detector only, as opposed to using the whole tracker including the silicon strip detector, allows for quick track reconstruction saving computing cycles. The UPC triggers were required to have at least one reconstructed pixel track in order to reject backgrounds where no particles ~~are~~were reconstructed by the tracker. For the muon trigger in Table 3.2 the rate was reduced by nearly a factor of 4 compared to its L1 seed rate in Table 3.1.

HLT trigger	Rate (Hz)	L1 prescale	HLT prescale	L1 seed	Type
L1UPCMuon and Pixel Track	0.52	1	1	1	Physics
L1UPCECAL2 and Pixel Track	1.65	2	1	2	
L1UPCECAL5 and Pixel Track	0.26	1	1	3	
L1ZDCOr	3.6	1500	11	4	Monitor
L1ZDCOr and Pixel Track	2.8	1500	1	4	
L1UPCMuonHFVeto and Pixel Track	0	off	off	5	Backup
L1UPCECAL2HFVeto and Pixel Track	0	off	off	6	
L1UPCECAL5HFVeto and Pixel Track	0	off	off	7	

Table 3.2: List of 2011 HLT trigger.

The total HLT output for the UPC trigger package was limited to 20 Hz. The limiting factor for the HLT rate was the amount of disk space given to this analysis. To meet the bandwidth requirements and collect a significant sample of data for estimating efficiencies, the prescales were balanced with the goal of achieving at least 5% statistical precision on the efficiency measurements. As an example of the balancing of the prescales, the HLT ZDC trigger that did not require a pixel track was given a additional prescale factor of 11 on the HLT. The ZDC path that also required a pixel track on the HLT, which used the same L1 seed, was only prescaled at the L1. The prescale of 11 was set to ensure that at least 1000 of the pixel track ZDC triggers overlapped with the ZDC L1 only triggers so that efficiency of the pixel track requirement in the trigger could be estimated

from the tracks lost.

3.3 Studies of 2011 PbPb data

The UPC triggers for the 2011 PbPb run make several studies possible. Three such studies are discussed below: $\gamma\gamma \rightarrow e^+e^-$, UPC interactions in peripheral nuclear collisions, and forward UPC J/ψ using HF.

3.3.1 High mass $\gamma\gamma \rightarrow e^+e^-$ in PbPb 2011

This measurement would make use of the electron triggers and combine the current dimuon data with dielectron data from the ECAL triggers. Because of the smaller mass of the electron, dielectron production is slightly favor compared to dimuon production. STARlight predicts that dielectron cross section is a factor of 2.5 higher in Xn break-up mode than for the dimuons channel when looking at masses above 4 GeV. The ECAL is position just beyond the tracker, whereas the muon system is the outermost sub-detector. This elevates the main reduction of muon acceptance, which is the material budget.

The contribution from higher order diagrams can be explored by studying photoproduction of dilepton pairs. Because the Pb nucleus has a charge 82 times higher than the proton, the electromagnetic coupling is stronger, and therefore, higher order terms is the perturbative expansion would potentially be more important. By measuring the cross section for $\gamma\gamma \rightarrow e^+e^-$, the extent to which higher order terms are needed in coherent photon coupling can be constrained. Recent results by ALICE favor very small contributions for higher order terms []. In addition, this analysis provides a useful cross check to the UPC quarkonia analysis such as J/ψ by verifying the cross section normalization.

3.3.2 UPC hadronic overlap

In the model calculations for UPC quarkonia photoproduction all hadronic interactions are rejected. However, inclusive p_T spectra of J/ψ measured by ALICE in peripheral PbPb collisions show a low momentum peak consistent with coherent photoproduction [?]. The ALICE spectra provide



Figure 3.1: Coherent excess in inclusive J/ψ p_T spectrum.

hints that UPC processes might also be present in peripheral nucleus-nucleus collisions at the LHC.

To study the overlap between photoproduction and hadronic production of quarkonium events, the inelastic sample and the UPC sample could both be used. The looseness of the rejection criteria to reject hadronic interactions, which uses the BSC detectors, leaves a significant overlap with peripheral hadronic collisions. The inclusive quarkonia sample from typical hadronic collisions can also be utilized. Coherent quarkonia photoproduction has a distinctive low p_T structure that can be used to identify photoproduced candidates in a sample that contains photoproduction combined with hadronic interactions. This measurement would open up the door to exploring the boundary between photoproduction and hadronic production.

3.3.3 UPC J/ψ with ~~muons~~electrons in HF

As higher rapidities are explored both lower and higher momentum partons of the nucleus are probed. Because these two contributions to the UPC photoproduction cross section can be separated using neutron tagging in incoherent events, exploring higher dimuon rapidities becomes attractive. HF extends to 5 in η , which is 2.6 units beyond the edge of the tracker. By combining hits in HF with tracks in the tracker ~~the higher dimuon rapidities could be explored~~, J/ψ from higher rapidities can be measured. When combined with neutron tagging of incoherently produced quarkonia, the current study can be extended to probe lower- x nuclear partons by identifying muons in HF.

3.4 Trigger development for the LHC pPb Run

Specific UPC triggers were also developed for the pPb run in 2013. For this period of running a much higher total trigger rate was read out relative to 2011. The total rate allocated for UPC triggers at the L1 in 2013 was 5 kHz and 50 Hz at the HLT. This factor of 5 increase in HLT and factor of 25 in L1 bandwidth, allowed for a change in emphasis from the L1 to the HLT.

The basic strategy in 2013 was the same as in 2012, use the loosest available ECAL and muon L1 triggers ~~to push~~ to capture the lowest p_T electrons and muons possible and reject hadronic interactions. Because of the L1 bandwidth restrictions in 2011, both the ZDCs and the BCSs were used on the L1 to reduce rates. In 2013 only the muon and ECAL triggers were used on the L1 allowing for rejection of hadronic interactions through cuts on track multiplicity. In addition, a more sophisticated trigger using full dimuon reconstructed was developed to increase purity. The main advantage in this shift in strategy was a higher purity due to the increased sophistication of the reconstruction on the HLT. In addition, an increase in cross section of the underlying physics process was achieved by relaxing the neutron emission requirement.

The HLT triggers in 2013 rejected hadronic interactions through counting tracks. For the five UPC trigger paths included in the HLT menu, three levels of reconstruction were done at the HLT.

- Pixel tracks were reconstructed from the inner pixel section of the silicon tracker alone, tracks were reconstructed using the full tracker using the strips as well, and full dimuon reconstruction was done using the tracker and muon detector.
- The least restrictive pixel track paths required at least one track reconstructed from the pixel detector and less than 10 pixel tracks in the event.
- Full tracking paths were added on top of the pixel track paths and included an additional requirement of one full track and less than 7 reconstructed tracks.
- The most restrictive path added to the pixel and full tracking paths and required reconstruction of dimuons with a mass between 2 and 12 GeV.

3.4.1 J/ψ photoproduction in ultra-peripheral pPb collisions

The CMS UPC triggers commissioned for the 2013 LHC pPb will allow for the study of J/ψ photoproduction. This process is dominated $\gamma - p$ interactions [?, ?]. The measurement would primarily probe the proton gluon densities. In Eq. ?? the photon flux depends on the square of the number of protons in parent nucleus, Z^2 . However, the cross section of the target only increase as the total number of nucleons to $A^{2/3}$. The much higher photon flux from the Pb-ion compensates for the decreased size of the proton.

A pPb UPC J/ψ measurement will complement the measurements done at HERA [?, ?, ?], and measurements done by ALICE [?]. CMS will contribute by adding additional kinematic coverage and cover a unique range of γp center of mass energies, $W_{\gamma p}$. The difference in beam energies and species at LHC versus HERA result in access to different $W_{\gamma p}$. ALICE and CMS have different acceptance in J/ψ rapidity, which also translates to coverage of different $W_{\gamma p}$. In addition, an excess in the UPC cross section compared to HERA measurements would indicate a non-exclusive contribution to the pPb UPC J/ψ cross section. This measurement will both help enhance the current understanding of the γp J/ψ photoproduction cross section as a function of $W_{\gamma p}$.

Chapter 4

Analysis

In this chapter the various parts of the analysis are explained. In Section 4.1, the simulations used to estimate the detector’s ability to measure UPC processes are discussed. The selection of UPC events is detailed in Section 4.2. Extraction of the number of coherent J/ψ candidates is explained in Section 4.3. The determination of the detector’s efficiency for measuring UPC events is explained in Section 4.4. Finally, [Section in Chapter ??](#) lays out the systematic uncertainties for the measurement.

4.1 Physics generators and Monte Carlo simulations

Every physical measurement is the product of the underlying physics folded with the response of the detector used to do the measurement. In order to understand the underlying physical process, the detector’s effect on the measurement must be understood and accounted for. As instruments become more and more complicated, the interplay among all of the many parts of the detector makes an analytic approach to the problem untenable. For this reason, the numerical technique of Monte Carlo (MC) simulation is often the most effective approach for describing detector effects.

MC simulations use random number generation to model the many statistical effects of particles interacting with different parts of the detector. First, particles are generated according to theoretical distributions. These particles are then propagated through a simulation of the detector. As the

particles pass through the detector, random numbers are used to determine how these particles interact with the materials of the detector based on the known properties of the material. In this way, the theoretical distributions are convolved with a realistic model of the detector's response. A more detailed picture of how the detector shapes the underlying distributions emerges with each successive event. The final goal of the MC simulation is to produce a set of events that accurately reproduce what would be measured if the theoretical input describes nature well.

4.1.1 MC and data comparisons

~~Comparison of the of the dimuon rapidity distributions between coherent MC sample and data.~~
~~Comparison of the of the dimuon ϕ distributions between coherent MC sample and data. Comparison~~
~~of the of the dimuon distributions between coherent MC sample and data.~~

4.1.1 STARlight and particle gun MC

In this thesis, two classes of generator input samples were used, STARlight [?, ?] and a particle gun. The STARlight samples correspond to the theoretical calculations described in Section ??, while the particle gun produces particles with a user defined transverse momentum distribution and rapidity distribution and isotropic decay to muon pairs in the J/ψ rest frame. For STARlight, three different physical process were simulated: coherent J/ψ production, where the photon couples to the nucleus as a whole; incoherent J/ψ production; where the photon couples to a single nucleon within the nucleus, and photon-photon interactions, where the photons from the two nuclei interact with each other to produce a pair of oppositely charge muons. All three STARlight samples contain a μ^+ and μ^- in the final state.

Because STARlight is not integrated into the standard CMS software framework (CMSSW), a simulation software chain with 5 steps was developed. First, STARlight is run in the specified mode, and a single file is created for each physics process. In step 2, the STARlight output file is converted to the Les Houches [Event](#) (LHE) format [?], and the momentum of the parent J/ψ or the initial photon-photon pair is added to the record of each event. The event record produced by

STARlight only contains the final state particles. To process the events in parallel, the STARlight files are subdivided in step 2, creating several LHE files from a single STARlight file. The LHE files are used as input to CMSSW.

Steps 3 to 5 take place within CMSSW. In step three the generated particles are propagated through the GEANT4 [?] detector simulation. This accounts for all the interactions with the detector and produces as output a format identical to the raw data that is recorded during data taking. Steps 4 and 5 are processed using the same software as in data taking. In step 4 the reconstruction software used during data taking is run on the output of the detector simulation. The output of the reconstruction is reduced to the information that is needed for the final analysis in the final step.

The particle gun samples were created entirely within CMSSW. J/ψ mesons were created according to user defined p_T and rapidity distributions. The decay of J/ψ s to a $\mu^+\mu^-$ pair was simulated with a uniform decay distribution, corresponding to unpolarized J/ψ particles. As with the STARlight samples, these muons are propagated through the GEANT4 simulation [?] of the detector, and the raw data is produced. The remaining steps of running the reconstruction code and reducing the data to the final data format needed for the analysis are identical to the STARlight production.

The momentum of the final state muons is the main driver of whether the candidate can be measured. One of the two daughter muons must have large enough momentum to fire the trigger, and both muons must have enough momentum to be reconstructed and tagged as a muon. There are at least 10 interaction lengths of material through which the muons must travel in order reach the muon chambers (see Fig. 1.11). This imposes an effective momentum threshold of about 7 GeV in order for muons can fire the trigger.

The p_T distribution and the polarization of the J/ψ s produced are the main factors controlling the momentum of the muon daughters, which vary for the different MC samples. The polarization effects how the momentum is shared between the daughters [?]. In the rest frame of the parent J/ψ , equal momentum is given to each daughter muon. However in the lab frame of the detector, the muon daughters which are emitted from transversely polarized J/ψ will tend to be emitted in

the direction the J/ψ is traveling and will have unequal momentum in the lab frame. The daughter traveling in the direction of the J/ψ will have increased momentum, whereas the daughter traveling opposite to the J/ψ direction will have decreased momentum.

In Fig. 4.1 the J/ψ 's p_T from the STARlight generated coherent, and incoherent, and the dimuon p_T for photon-photon samples are compared. Both the coherent and the photon-photon samples are concentrated a low p_T , and neither sample extends much beyond 0.15 GeV. The incoherent sample is peaked near 0.5 GeV and extends beyond 1 GeV. The two particle gun samples resemble the incoherent and coherent samples p_T distributions. The first sample has a Gaussian p_T distribution extending to approximately 0.15 GeV, whereas the second is flat in p_T up to 2 GeV.

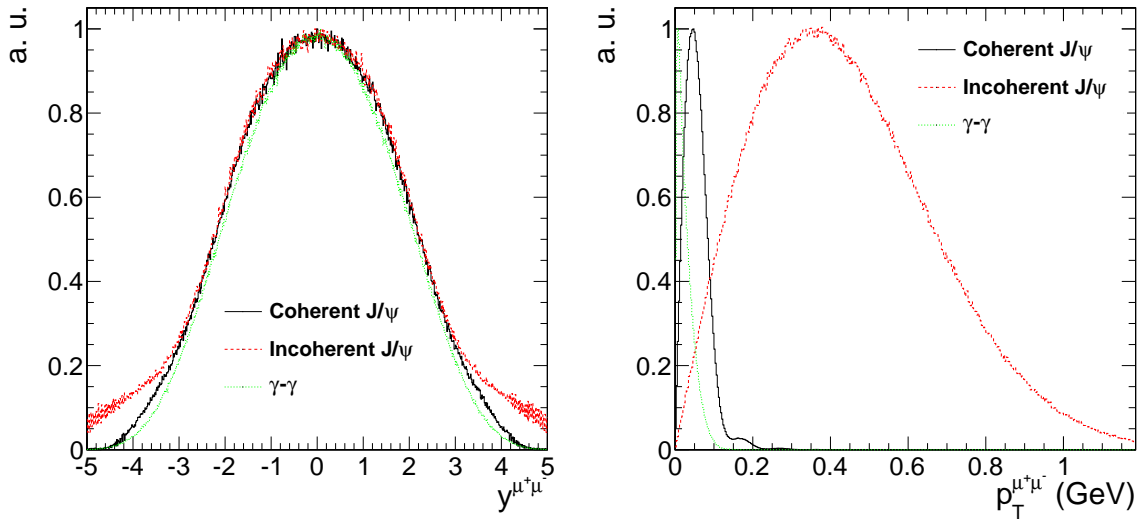


Figure 4.1: Generator level rapidity (left) and p_T (right) distributions for the coherent (black), incoherent (red), and photon-photon process (green).

The particle gun samples are unpolarized, whereas the STARlight samples have transverse polarization. In Fig. 4.2, the cosine of the helicity angle of the particle gun samples and the STARlight samples are shown. For the STARlight sample the helicity angle, the angle between the direction of the μ^+ daughter and the J/ψ direction in the rest frame of the J/ψ , prefer to be either parallel or anti-parallel. However, the particle gun samples have no preferred direction of emission.

[Figures 4.3, fig:jpsiPhiCoherent](#) show the rapidity, ϕ , and p_T distributions of reconstructed

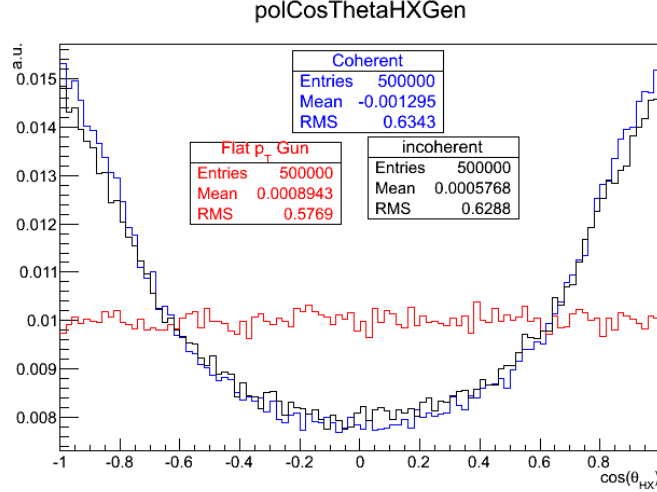


Figure 4.2: The J/ψ polarization of the particle gun (red), coherent (blue), and incoherent samples are plotted as the cosine of the helicity angle.

coherent J/ψ MC from STARLight and data. All distributions are normalized to unity. The rapidity distribution of the STARLight is very slightly higher than for the data, with a difference in the mean rapidity of ≈ 0.1 unit. The ϕ , and p_T distributions for STARLight and data are both very similar.

4.2 Event selection

The unprecedented amounts of data produced by the LHC has made it possible to investigate novel physics processes like UPC J/ψ production. The data for this analysis were recorded during the 2011 LHC PbPb run. During this period, $150 \mu b^{-1}$ were recorded by the CMS detector, corresponding to over a billion PbPb collisions. Of this, $143 \pm 7 \text{ (syst)} \mu b^{-1}$ of data were used in this analysis due to the ZDCs being temporally disconnected to test the Forward Shower Counters.

4.2.1 Data sets

The data were divided into three specially selected samples, Physics, Monitoring, and Zero bias, based on the triggers which recorded the events (see Table 4.1). By recording this hierarchy of samples, interesting events are selected with a much higher purity in the physics sample, while

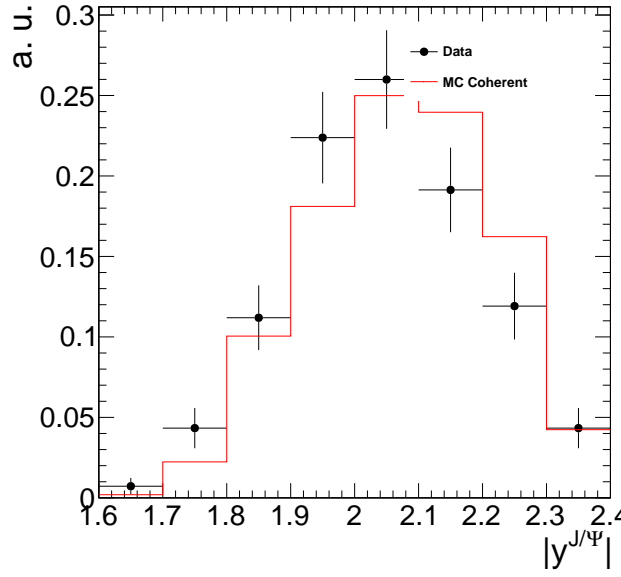


Figure 4.3: Comparison of the of the dimuon rapidity distributions between coherent J/ψ MC sample and data.

the zero bias and ZDC triggered samples allow for the investigation of the selection criteria. The purity, which is a measure of how many signal events relative to background events are in an sample, is obtained by using more selective triggers. Less selective triggers, those assigned to the monitoring and zero bias samples, were used to investigate to what extent signal events are lost due to the higher selectivity of physics triggers. These samples were recorded using subsets of the HLT triggers found in Table 3.2 of Chapter 3. The J/ψ events discussed in this thesis were obtained by analyzing the sample labeled in Table 4.1 as physics. A ZDC triggered monitoring sample was recorded for the sake of estimating efficiencies. Lastly, a zero bias sample was recored for investigating the ZDC and the noise distributions of HF.

The physics sample containing the J/ψ signal was recorded by the muon trigger labeled “L1UPCMuon and Pixel Track” in Table 3.2. Because of the characteristically low momentum of UPC J/ψ as compared to J/ψ created by other physics processes, the loosest muon trigger was used. The noise trigger rate for the muon trigger alone was 50 Hz, but in coincidence with the BCS veto and the ZDC trigger the noise rate was below 2 Hz. By pairing the muon trigger with the ZDC on the L1, the noise contribution was reduced from the noise contribution from either of the two sub-detectors

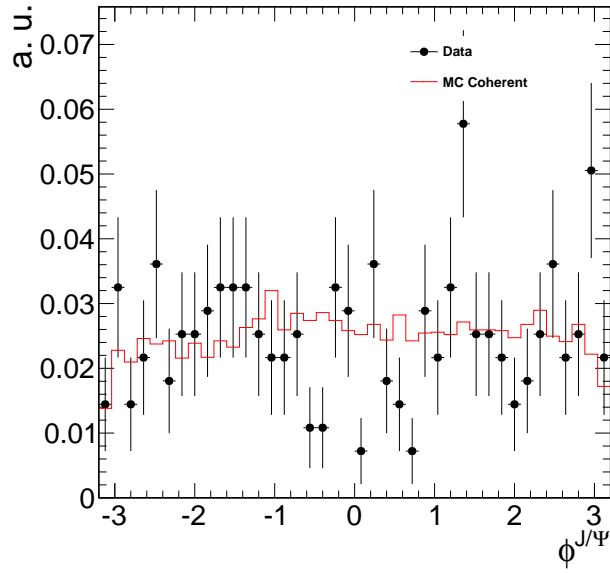


Figure 4.4: Comparison of the of the dimuon ϕ distributions between coherent J/ψ MC sample and data.

to the noise coincidence between the two sub-detectors. Contributions from hadronic interactions
~~are~~ were reduced by the veto on the BSCs. This trigger was designed to balance reducing the rate
 with maximizing the efficiency, allowing for the data to be recorded without producing high rates
 that would have resulted in dead time for the detector.

In order to investigate the muon trigger and the other parts of the event selection, a monitoring
 sample was recorded by requiring energy consistent with at least one neutron in either of the ZDCs.
 Neutron production is a much more common process than the UPC J/ψ production. This process
 has cross sections on the order of ~~100~~ 200 b compared to 10 mb predicted for J/ψ production.
 For this reason, the rates of this trigger are much higher than the physics trigger, and only a small
 sub set of these events are recorded. From this trigger the pixel track portion of the HLT trigger
 efficiency was estimated as well as the ZDC trigger efficiency, as will be described in Section 4.4.

In addition to the monitoring and physics sample, a zero bias sample was recorded to examine
 the ZDC neutron reconstruction and the HF noise distributions. The zero bias trigger fired every
 time both beams passed through CMS. Only 4 events out of every million triggered were recorded
 for this sample. This sample allowed for an unbiased measurement of the ZDC neutron threshold

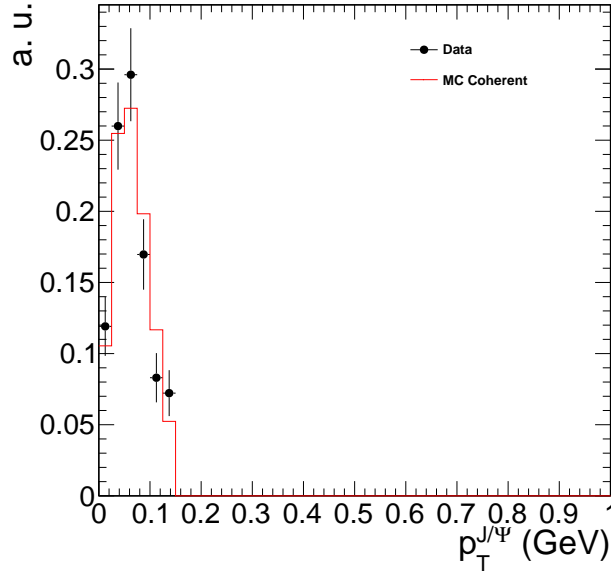


Figure 4.5: Comparison of the of the dimuon p_T distributions between coherent J/ψ MC sample and data.

Sample	Events	\mathcal{L}_{int}
Physics	346K	$143.3 \mu b^{-1}$
Monitor	1.1M	$31.6 mb^{-1}$
Zero Bias	8.8M	$580 b^{-1}$

Table 4.1: Integrated luminosities and number of events for the three samples used in this analysis.

energies as discussed in Section 2.1. Because the zero bias trigger only requires the presents of both LHC beams, the sample contains very few hadronic collisions. This allowed for a measurement of the electronic noise distribution in the HF, which are important to reducing contamination from hadronic interactions.

The integrated luminosity for each of the three samples is calculated by recording activity in HF [?]. The cross section for HF activity is measured from a van der Meer scan. In this way, the amount of integrated luminosity for any running period is related to the activity in HF.

4.2.2 Event selection cuts

The analysis described in this thesis focuses on UPC J/ψ s decaying to muons. The trigger used for this analysis ~~recored~~recorded 346841 events. A set of off-line cuts were applied to increase

the relative contribution of UPC events to background processes. Two sets of event selection cuts were applied to reject background events. The first set rejects background from the beam. The second rejects events where hadronic collisions have occurred. Table 4.2 summarizes all the event selection cuts.

Cut type	Cut	Events
–	all triggered	346841
beam background rejection	good vertex requirement	340997
	beam halo muon rejection	302777
	cluster shape compatibility requirement	233590
hadronic interaction rejection	single-sided neutron requirement	149992
	two track requirement	32732
	HF signal rejection	5392
fake muon rejection	muon quality requirement	2047
kinematic cut	J/ψ mass requirement	696
	muon detectability cuts	567

Table 4.2: Effects of event selection cuts.

To reject beam induced background the following cuts were applied:

- The reconstructed vertex must be within 2 cm in the transverse direction and 25 cm in the longitudinal direction. This cut ensures that reconstructed particles come from interactions between the two beams rather than event where one of the two beams interact with gas particles near the interaction point.
- Beam halo muons were rejected using the timing of the muon hits. The beam halo cut rejects events where muons surrounding the beam stream through the detector.
- Pixel cluster shape should be compatible with the vertex. This cut requires that energy deposits in the silicon tracker point back to the reconstructed primary vertex.

These beam background cuts do not reject any UPC J/ψ candidates.

The second set of background rejection cuts were designed to reduce contamination from hadronic interactions.

- No more than 2 reconstructed tracks in the event. The track requirement rejects events that produce many charged particles.
- Maximum reconstructed hit energy in HF was required to be below the threshold for electronic noise. Nearly all hadronic interactions (about 98%) produce particles in the range $3 < |\eta| < 5$ covered by the HF detector. By requiring that the energy deposits in HF resemble noise, nearly all ~~elastic~~inelastic hadronic collisions are expected to be rejected.
- Energy in the ZDCs consistent with neutrons on only one side of the interaction point. In hadronic interactions both nuclei break-up. By requiring that ZDC only reconstruct neutrons on one side of the interaction point, hadronic interactions that produce neutrons on both sides were rejected.

Each of these cuts were designed to reject topologies produced by hadronic interactions. The effect of these cuts can be seen in Table 4.2 and are denoted hadronic interaction rejection.

To establish the HF noise thresholds, the noise distributions were measured in zero bias events. An offline selection of events with no reconstructed tracks was used to ensure that no collision had taken place. The HF noise threshold was defined as the cut that keeps 99% of the zero bias events. The noise distribution from this zero bias sample is compared to the physics sample and MC in Fig. 4.6.

The following standard muon quality cuts are applied:

- Tracker track matched with at least one muon segment (in any station) in both X and Y coordinates ($< 3 \sigma$).
- Cut on number of tracker layers with hits > 5 .
- Number of pixel layers > 0 .
- The χ^2 per degrees of freedom of the track fit < 3 .
- Loose transverse and longitudinal impact parameter cuts, within 3 cm in the transverse direction and within 30 cm in the longitudinal direction with respect to the primary vertex.

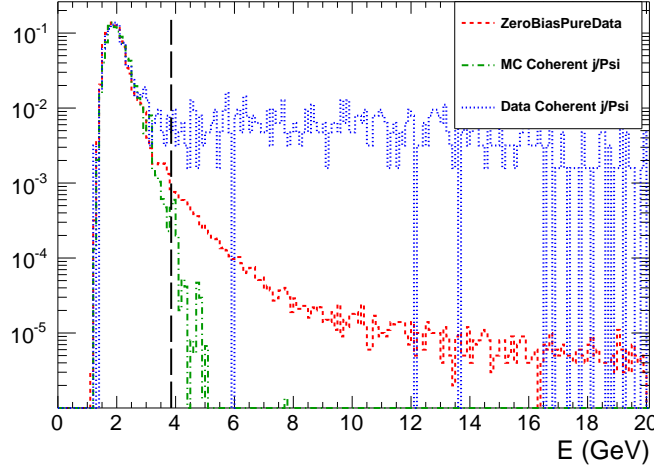


Figure 4.6: Comparison of HF noise distributions in zero bias data, physics triggered data, and MC.

These cuts are applied to reduce the number of fake muons and have been validated for other muon analyses [?].

4.3 Signal extraction

After all event selection cuts, the remaining events contain a combination of coherent J/ψ , incoherent J/ψ , and dimuons from the photon-photon process. Each process must be separated from the final mix. To achieve this, the invariant mass and p_T distributions are used to distinguish between the three processes. The photon-photon process is extended in invariant mass whereas the J/ψ is peak strongly near 3.1 GeV. In dimuon transverse momentum distribution of the photon-photon and coherent process have similar distributions, both peaked sharply below 0.1 GeV, whereas the incoherent process is more broadly distributed across an interval extending to nearly 1 GeV. The mass distribution was fit to separate the photon-photon process from the J/ψ process. The p_T distribution was used to separate the incoherent process from the photon-photon process, and the coherent process. In this way, a separate yield was extracted for all three processes.

The invariant mass distribution for opposite sign dimuons is shown in Fig. 4.7. A J/ψ signal is clearly visible together with tails at higher and lower mass due to the photon-photon process. A

686 fit to the invariant mass distribution was performed using a Gaussian to account for the J/ψ signal
 687 and a first-order polynomial function for the photon-photon process. The extracted number of J/ψ
 688 candidates from this fit includes all J/ψ s in the mass window that passed the analysis cuts, i.e.
 689 both coherent and incoherent process contribute to yield from the mass fit. The p_T distribution is
 690 needed to separate the two different contributions to the J/ψ peak.

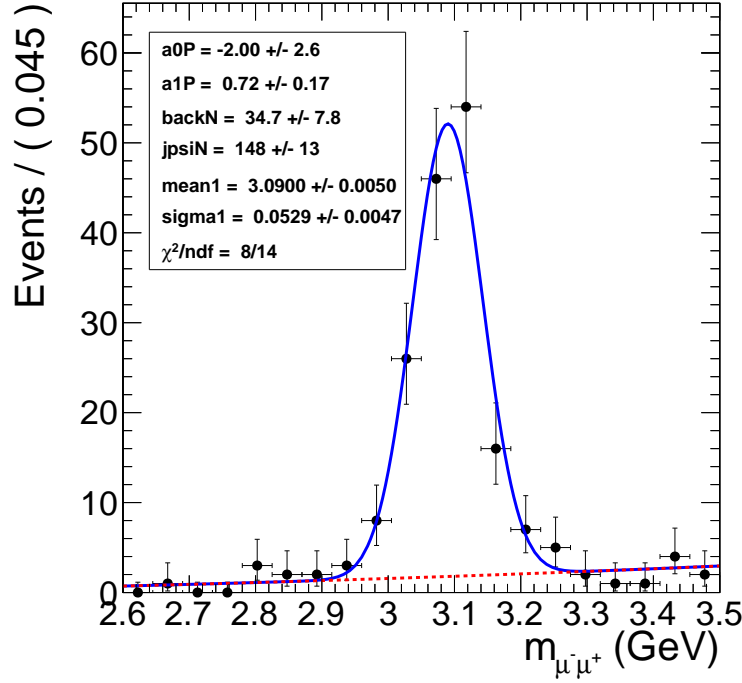


Figure 4.7: Mass fit to J/ψ using Gaussian for the signal and a first-order polynomial for the photon-photon continuum.

691 Figure 4.8 shows the p_T spectrum of the events plotted in Fig. 4.7. There is a clear coherent
 692 peak at $p_T = 60$ MeV followed by broad distribution that peaks near $p_T = 450$ MeV. To extract
 693 the contribution of coherent, incoherent and gamma-gamma processes in the data the spectrum
 694 in Fig. 4.8 was fit to the sum of three MC templates corresponding to the final output of the MC
 695 simulations for these three processes. The clear overlap of the coherent and photon-photon process,
 696 and the clear separation of these two lower p_T processes from the incoherent process is apparent.
 697 The shape of the p_T distribution for the coherent, incoherent, and photon-photon process are taken
 698 from the final output of MC after applying all analysis cuts. In Fig.4.8, the yield parameters that

were fit were left unconstrained for all three process.

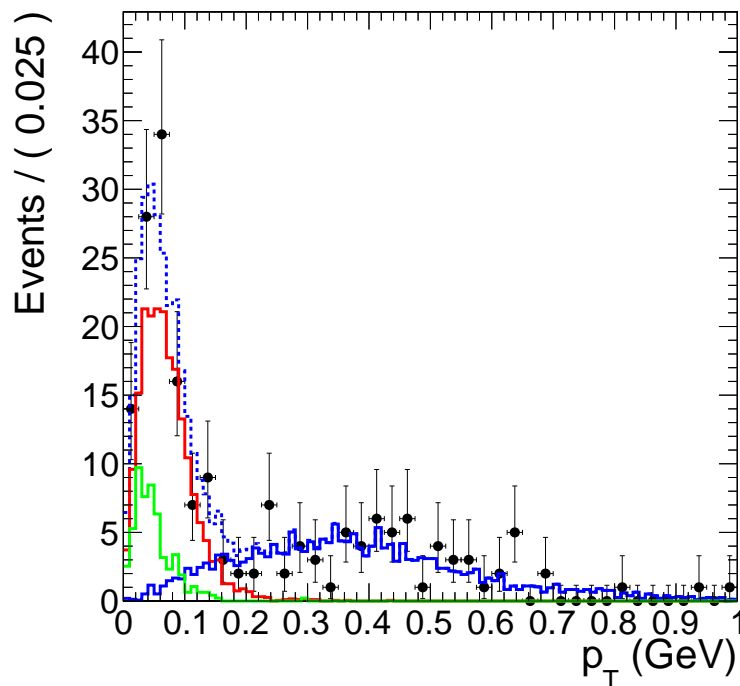


Figure 4.8: Fit to MC p_T templates.

The shape of the photon-photon and coherent J/ψ process are very similar in transverse momentum. Accordingly, the contribution from the photon-photon process and the coherent process are difficult to separate from the p_T distribution. The confidence contours in Fig. 4.9 from the template fit in Fig. 4.8 demonstrate the strong anti-correlation between the coherent yield parameter, nCo , and the yield parameter for the photon-photon process, $nGamma$. Because of the anti-correlation, the statistical uncertainty on nCo and $nGamma$ from the fit are larger than \sqrt{nCo} and \sqrt{nGamma} expected from Poisson statistics. The information from the invariant mass and p_T distributions were combined to break this correlation. Through this combination, the contribution to the final yield from the three process was measured.

A simultaneous fit to the mass spectrum and p_T spectrum was performed to utilize the mass fits ability to distinguish the photon-photon process from the coherent and incoherent process all while utilizing the p_T fits ability to separate the coherent and photon-photon processes from the incoherent. Fig. 4.10 shows the result of the simultaneous fit. The simultaneous fit forces the

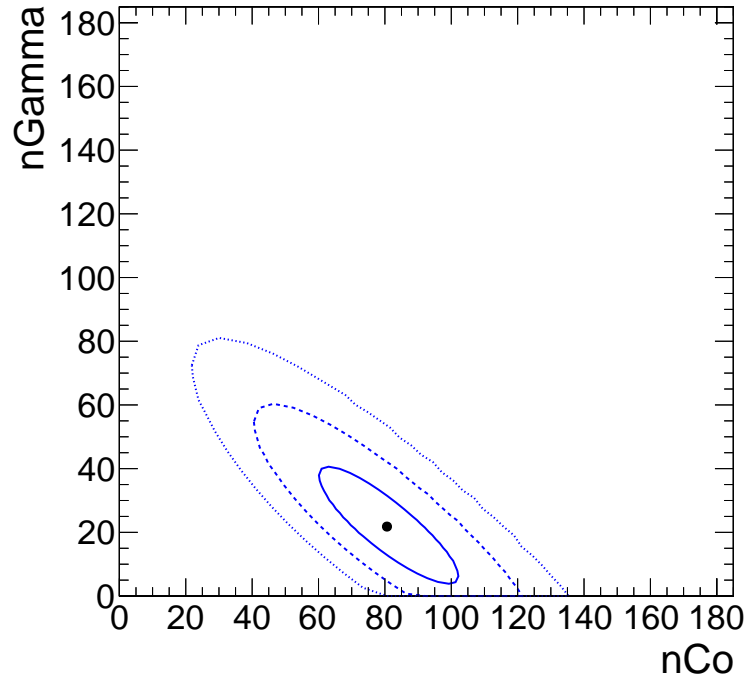


Figure 4.9: 68%, 95%, and 99% confidence contours from the p_T template fit.

parameter $nGamma$ to both describe the photon-photon continuum present in the side bands of the J/ψ mass peak as well the photon-photon contribution to the low- p_T part of the p_T spectrum. In addition, the J/ψ yield from the mass fit is forced to equal the contribution from the incoherent and coherent process in the fit to the p_T distribution. In this way, the correlation between the yield parameters was broken, and the contribution from the three process were made independent of each other.

Fig. 4.11 shows the confidence contours for nCo and $nGamma$ from the simultaneous fit in Fig. 4.10. The slope of the confidence contours in Fig. 4.11 is noticeably than in Fig. 4.9. The contours for the simultaneous fit are also reduced compared to Fig. 4.9 with widths in nCo and $nGamma$ similar to those expected from Poisson statistics. From the simultaneous fit, reasonable statistical errors were obtained along with the yields for the three processes.

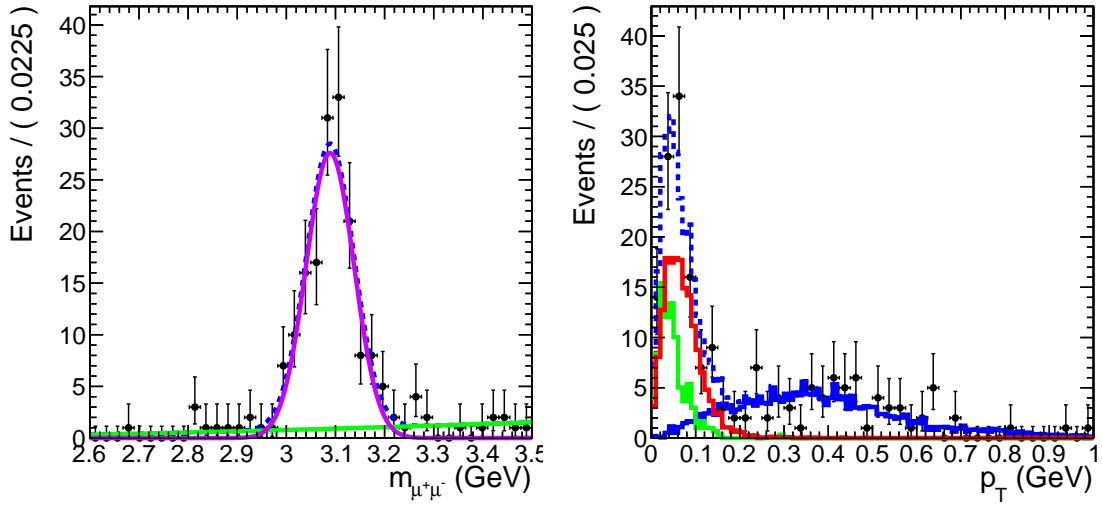


Figure 4.10: Simultaneous fit to the mass and p_T spectra.

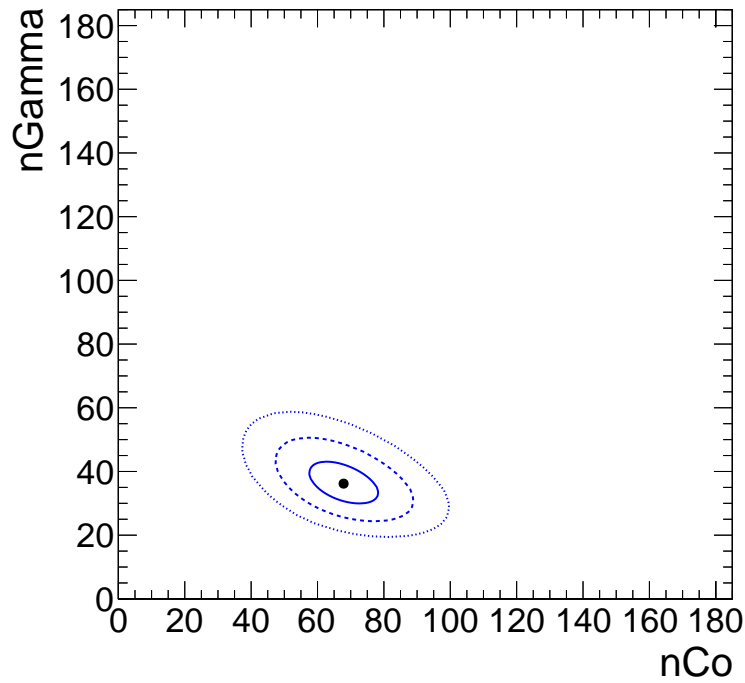


Figure 4.11: 68%, 95%, and 99% confidence contours from the simultaneous fit.

4.4 Efficiency determination

Each step of the triggering, event selection, and analysis has an associated efficiency that must be accounted for in the measurement of the J/ψ cross section. The ZDC trigger efficiency, the muon trigger efficiency, and the muon reconstruction efficiency are the two most significant contributors

to the total efficiency measurement. The efficiency of the pixel track requirement, and the veto on activity in the BSCs from the trigger are also estimated but found to be consistent with fully efficient. The following section explains how each of these efficiencies were measured with a special emphasis on the ZDC trigger efficiency and the muon trigger and reconstruction efficiencies.

4.4.1 Muon efficiencies

The muon efficiencies were measured using a combination of MC and data based methods. The MC based measurement accounts for the detector acceptance and the efficiency of the muon quality cuts discussed in Section 4.2. The trigger efficiencies were measured in data using the tag and probe method [?], which is discussed below.

CMS has a limited acceptance for J/ψ s, particularly in the case of J/ψ s with low momentum like those produced in UPC events. To measure the acceptance of CMS for J/ψ s, reconstructed dimuon candidates were considered detectable if both reconstructed muon daughters fell into a detectability region in p_T and η . The muon detectability region was defined using the coherent J/ψ events obtained from STARlight. The efficiency for reconstructing single muons ϵ_{reco}^μ is defined by $\epsilon_{reco}^\mu = \frac{N_{reco}^\mu}{N_{gen}^\mu}$, where N_{reco}^μ is the number reconstructed muons obtained after the full CMS detector simulation and that passed the standard muon quality cuts, and N_{gen}^μ is the number of generated muons from STARlight. Fig. 4.12 shows the efficiency for reconstructing single muons from coherent J/ψ events. To avoid the edges of the detectors acceptance, all reconstructed muons that fall into a $(p_T, |\eta|)$ bin that has an efficiency less than 20% were rejected. This condition defines the detectability region. The acceptance and reconstruction efficiency for reconstructing dimuons was calculated from MC using the following formula:

$$A \times \epsilon = \frac{N_{det}(|y|, p_T)}{N_{gen}(|y|, p_T)} \frac{N_{det}(|y|)}{N_{gen}(|y|)}, \quad (4.1)$$

where N_{det} is the number of reconstructed dimuons where both daughters fall into the detectability region, and N_{gen} is the number of generated dimuons. From Eq. 4.1, the acceptance for J/ψ was

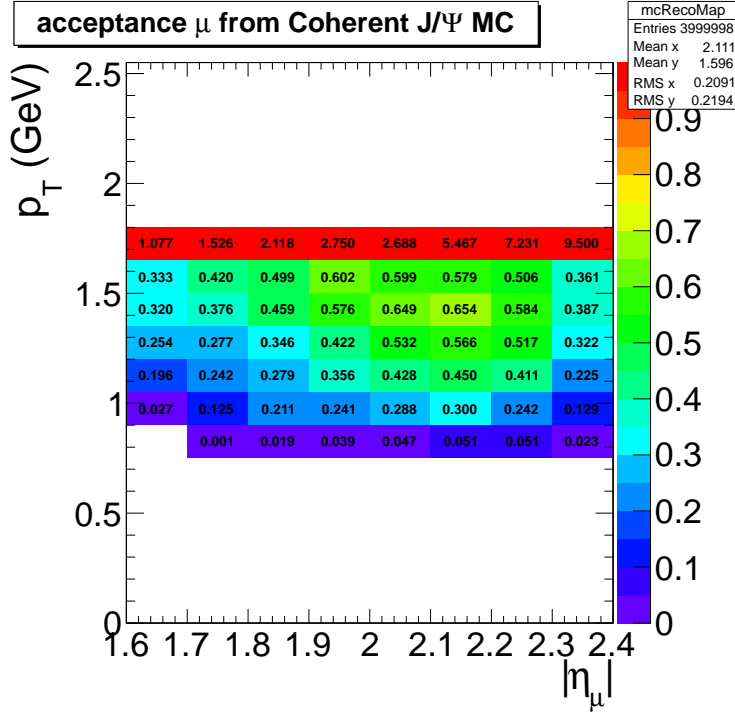


Figure 4.12: Muon daughter detectability from coherent J/ψ

calculated as a function of $|y|$, and p_T (see Fig. ??).

The “tag and probe method” is a data driven approach used to measure the trigger efficiency of the muon daughters from J/ψ decays. In this method there are three categories of daughter muons. *Tag muons* are high quality muons. *Passing probes* are reconstructed muons that match the muon trigger, while *failing probes* do not. Each dimuon will have one daughter classified as a tag and the other as a probe. From here three invariant mass histograms are studied. One histogram is created from all pairs. The second comes from pairs where the probe is a passing probe. The last histogram comes from pairs where the probe fails to fulfill the trigger, it is a failing probe. By matching the tag to the trigger, the probe is unbiased by the trigger and the efficiency can be measured by fitting the three mass histograms.

Because the trigger efficiency depends on the p_T and $|\eta|$ of the muon, one set of three histograms for each $(p_T, |\eta|)$ bin of the probe is created. To extract the single muon trigger efficiency ϵ_{trig}^μ , each set of invariant mass histograms were simultaneously fit. The signal was fit using a Crystal Ball function, and the background was fit to an exponential. The Crystal Ball parameters

were simultaneously fit to all three histograms. The exponential function was fit to the failing and passing probe histograms separately. Because the background shapes are in principle different for the two samples, the efficiency is driven by this difference.

Fig. 4.14 shows the fit of the three sets of pairs. This fit was done for each bin of the probes p_T

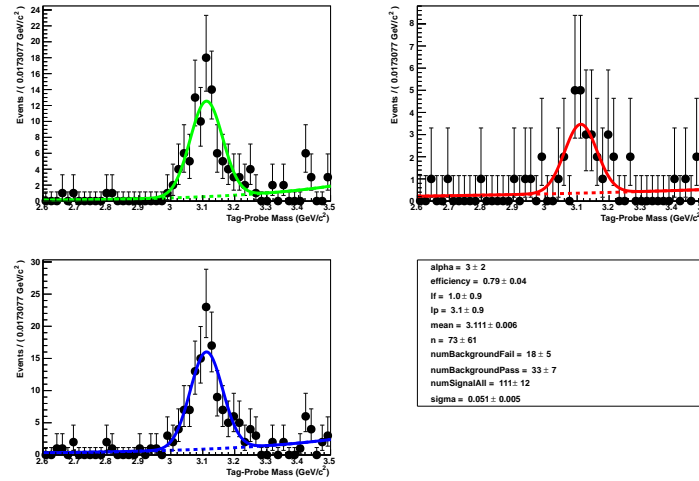


Figure 4.14: Fits to tag and probe pairs in the J/ψ mass region for pairs with a probe $2 < |\eta| < 2.2$ and $1.55 < p_T < 1.8$ GeV.

and η . The efficiency from the fits in each bin are shown in Fig. 4.15.

The dimuon trigger efficiency $\epsilon_{trigger}^{dimuon}$ was calculated from the single muon efficiencies using the following equation:

$$\epsilon_{trigger}^{dimuon} = 1 - (1 - \epsilon_{trigger}^{\mu_1})(1 - \epsilon_{trigger}^{\mu_2}), \quad (4.2)$$

where $\epsilon_{trigger}^{\mu_1}$ is the tag and probe efficiency of the first dimuon daughter, and $\epsilon_{trigger}^{\mu_2}$ is the efficiency of the second muon daughter. In Eq. 4.2 the probability of at least one daughter firing the trigger is calculated by subtracting one from the probability that neither daughter fires the trigger, thus giving the dimuon trigger efficiency.

The average dimuon trigger efficiency for each dimuon $(\sqrt{s}, |y|)$ bin was calculated by averaging the efficiency of dimuon candidates in each bin. The dimuon trigger efficiency ranges from about 50% to 90%. As expected the J/ψ trigger efficiency ~~increase~~ increases with rapidity since the longitudinal momentum of the J/ψ is given by $p_Z = M_{J/\psi} \cdot \sinh(y)$. Thus J/ψ mesons at forward

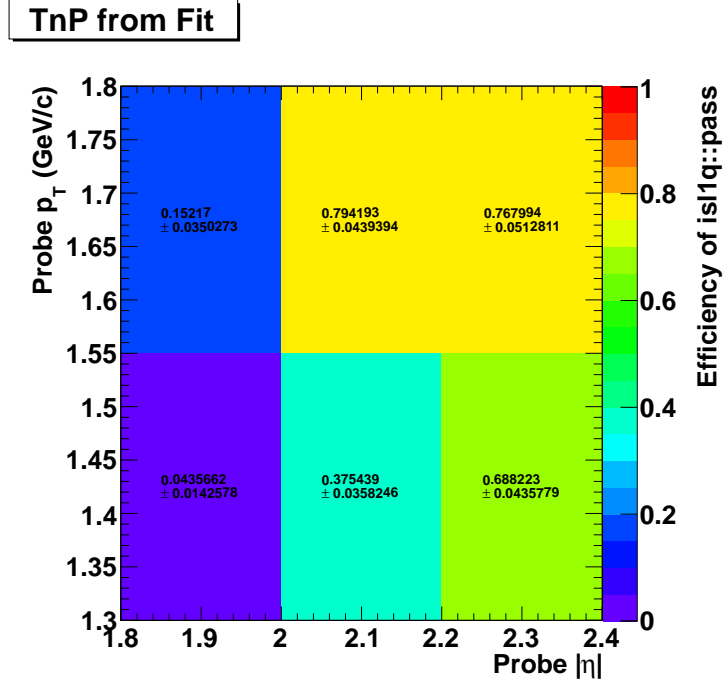


Figure 4.15: Muon trigger efficiencies in p_T and η bins from the tag and probe method.

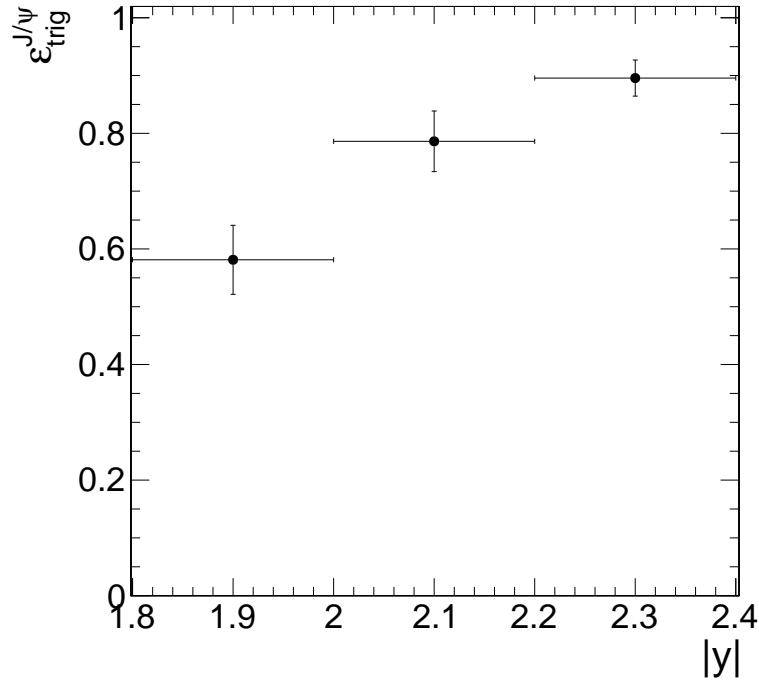


Figure 4.16: The trigger efficiency from tag and probe averaged over candidates in each $|y|$ bin.

rapidity distribute more momentum to their daughter muons which therefore have a greater chance of punching through into the muon chamber. The average trigger efficiency was multiplied by the acceptance and reconstruction efficiency from the MC to produce a total factor for both efficiency and acceptance.

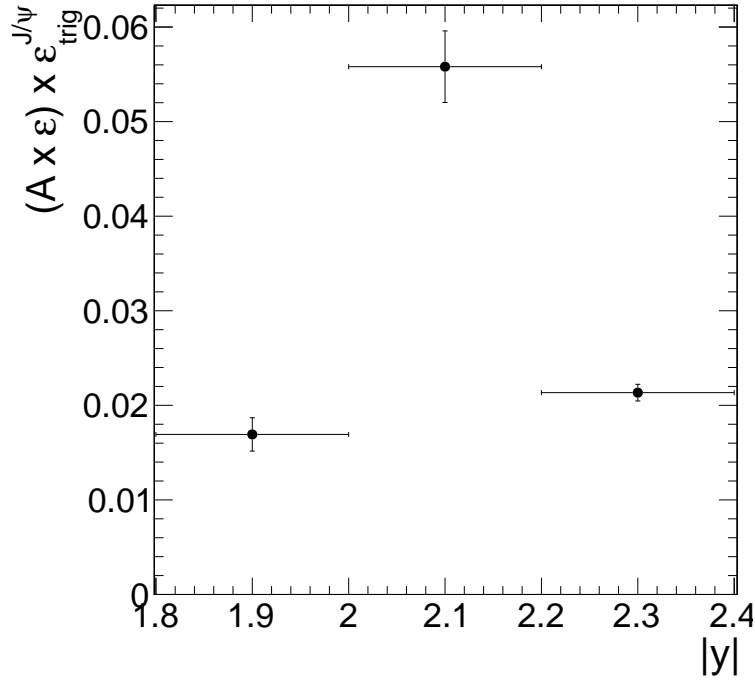


Figure 4.17: The acceptance times averaged trigger efficiency from tag and probe.

The total combined efficiency and acceptance factor for coherent J/ψ between $2.0 \leq |y| \leq 2.2$ was found to be $\approx 5\%$. The acceptance factor of roughly 7% from the MC was found to be the main contributor to the total efficiency. The interplay of the polarization of the J/ψ and the material in detector drive drives down the efficiency by creating an effective momentum threshold for detection (see Section 4.1). The reconstruction efficiency of the daughters range between 20%-60% for muons in the defined detectability range. The trigger efficiency for the detectable muons ranges from 30%-80% depending on p_T .

ZDC Side	N_{events}	N_{trig}	ϵ_{ZDC}
ZDC ⁺	73028	71706	$0.9819 \pm \textcolor{red}{0.005} \textcolor{blue}{-0.0037}$
ZDC ⁻	76132	71859	$0.9439 \pm \textcolor{red}{0.005} \textcolor{blue}{-0.0035}$

Table 4.3: ZDC trigger efficiencies for ZDC reconstruction method 1 and 2

4.4.2 ZDC trigger efficiency

As discussed in Section 2.1, the trigger labeled "L1ZDCOr and Pixel Track" in Table 3.2 was used to measure the ZDC trigger efficiency. This trigger required either a ZDC⁺ or ZDC⁻ trigger, together with at least one pixel track. The veto on the BSC minimum bias trigger, as in the physics triggers, was applied offline. The BSC veto excludes events where BSCs from both sides of the interaction point are above threshold. This trigger was used in order to collect the most inclusive possible sample without using the minimum bias triggers designed to collect hadronic interactions.

This ZDC triggered sample suffers from a trigger bias. For example, a sample triggered by ZDC⁺ would always produce a ZDC⁺ trigger efficiency of one. To avoid this, a similar technique to tag and probe was used. Each event is either tagged as triggered by ZDC⁺ or triggered by the ZDC⁻. The ZDC⁺ trigger efficiency is measured from the ZDC⁻ tagged sample, and vice versa.

To estimate the efficiency, the number of events with energy in ZDC⁺ greater than the single neutron threshold, N_{events} , was measured. From this set of events, the number of events that also fire the ZDC⁺, N_{trig} , was measured. The ratio between the number of single neutron events that fired the trigger and all single neutron events was taken as the estimate of trigger efficiency. The same procedure was applied for each side of the ZDC. The trigger efficiency was found to be 98% for ZDC⁻ and 94% for ZDC⁺.

Chapter 5

Results and summary

In the previous two chapters the analysis steps to measure the coherent J/ψ photoproduction were given. In this chapter, the measured cross section for this process is given in Section 5.1. Comparisons to the theoretical models are discussed. In addition, the rapidity correlation between UPC J/ψ and forward neutrons are presented and compared to model calculations in Section 5.2. Finally, a summary of the complete thesis is given.

5.1 Coherent J/ψ cross section

The coherent J/ψ cross section is calculated using the following formula:

$$\frac{d\sigma_{coh}^{J/\psi}}{dy}(Xn0n) = \frac{N_{coh}^{J/\psi}}{\mathcal{L} \cdot (2 \cdot \Delta y) \cdot BR}, \quad (5.1)$$

where $N_{coh}^{J/\psi}$ is the corrected number of coherent J/ψ candidates, \mathcal{L} is the integrated luminosity used for this analysis, Δy is the width of the rapidity interval, and BR is the branching ratio for J/ψ to $\mu^+\mu^-$. To obtain $N_{coh}^{J/\psi}$ the following formula was used:

$$N_{coh}^{J/\psi}(Xn0n) = \frac{N_{yield}^{J/\psi}}{(A \times \epsilon) \cdot \epsilon_{trig}^{ZDC} \cdot \epsilon_{trig}^{J/\psi}}, \quad (5.2)$$

$N_{yield}^{J/\psi}$	65 ± 12	$N_{coh}^{J/\psi}$	1180 1213 ± 220 240
$A \times \varepsilon$	0.0725 0.07	\mathcal{L}	143.3 ± 7.2 143
ε_{trig}^{ZDC}	0.96	BR	0.0593
$\varepsilon_{trig}^{J/\psi}$	0.79 ± 0.05	Δy	0.2
$N_{coh}^{J/\psi}(Xn0n)$	1180 1213 ± 220 240	$\frac{d\sigma_{coh}^{J/\psi}}{dy}(Xn0n)$	347.7 356 ± 71 (stat) $^{+43}_{-50}$ (syst) μb

Table 5.1: The measured quantities used to calculate the corrected number of coherent J/ψ , $N_{coh}^{J/\psi}(Xn0n)$ (right), and the quantities used to calculate the cross section for UPC J/ψ photo-production, $\frac{d\sigma_{coh}^{J/\psi}}{dy}(Xn0n)$ (left).

where $N_{yield}^{J/\psi}$ is the J/ψ yield with a $p_T < 0.15$ GeV, $A \times \varepsilon$ is the combined acceptance and efficiency, ε_{trig}^{ZDC} is the ZDC triggering efficiency for detecting at least one neutron emitted in the forward region, and $\varepsilon_{trig}^{J/\psi}$ is the J/ψ trigger efficiency measured by the “tag and probe” method. Each of these quantities can be found in Table 5.1.

The coherent J/ψ cross section $\frac{d\sigma_{coh}^{J/\psi}}{dy}(Xn0n)$ ~~includes the emission of at least one neutron emitted~~requires single-sided neutron emission, $Xn0n$. Previous measurements carried by the ALICE Collaboration measured the cross section without any break-up requirement. In order to compare to their results, the cross section is scaled by the factor 5.06 to account for the increase in cross section. This value was obtained from STARlight. The resulting cross section is ~~1.76 ± 0.22~~ 1.80 ± 0.37 (stat) $^{+0.22}_{-0.25}$ (syst) mb.

~~Figure X-~~ Figure 5.1 shows the measured cross section compared to the ALICE data points, as well as STARlight, AB and LTA models (see Chapter ??). The measured cross section is in agreement with previous measurements, and favors the AB-EPS09 model. Given the measured cross section is significantly below STARlight, nuclear gluon shadowing plays an important role for $x \sim 10^{-2}$.

5.2 UPC J/ψ -neutron rapidity correlation

In addition to the production cross section, neutron dependent J/ψ photoproduction can be studied in order to better understand the separation between coherent and incoherent photoproduction. Be-

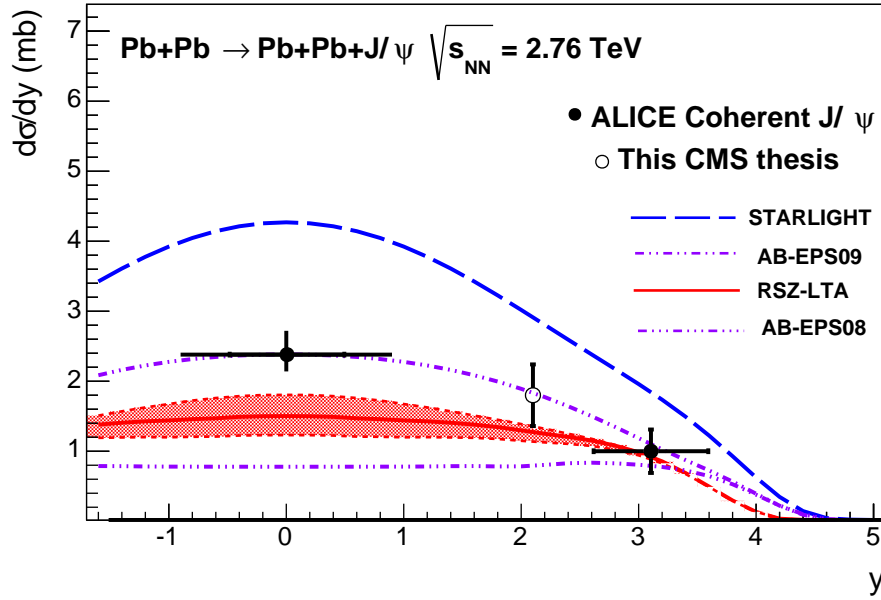


Figure 5.1: Coherent J/ψ photoproduction cross section measured by ALICE and CMS including feed-down and rescaled for nuclear break-up.

cause of the inclusion of the ZDC in the trigger, the data for this thesis is well suited for studying the correlations between the J/ψ and neutron rapidities. The difference between neutron emission in coherent and incoherent production was studied in the past [?], and recent studies have explored what is possible within the acceptance of CMS [?]. In this section, the ratio between J/ψ s produced with neutrons in the same side of the detector and opposite side of the detector will be shown and compared with theory.

Figure 5.2 shows the rapidity distribution of UPC J/ψ that are accompanied by neutron detection on only one side of the interaction point. The candidates are divided by p_T and the side of the interaction point the neutron was detected in. Low- p_T corresponds to the $p_T < 0.15$ GeV, and high p_T corresponds to $0.15 \text{ GeV} < p_T < 1 \text{ GeV}$. The filled black circles correspond to candidates that are ~~produce~~-produced in conjunction with a neutron in ZDC^- , whereas the open squares indicate a neutron in ZDC^+ . In Fig. 5.2, there is a clear preference for the neutron and J/ψ to be detected in the same side of the detector for the high- p_T candidates, however the low- p_T candidates do not show a strong preference.

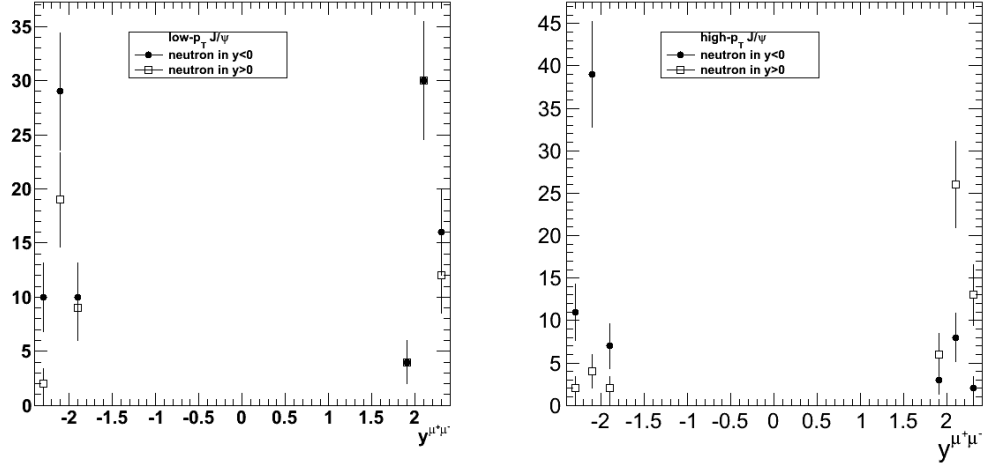


Figure 5.2: Rapidity distribution of J/ψ in the case of the events having the neutron in negative and positive rapidity for the low- p_T J/ψ (left), high- p_T J/ψ (right) and dimuons from $\gamma\gamma$ sample (bottom).

The ratio between candidates with neutrons on the opposite side of the detector and candidates with neutrons on the same side of the detector, $R_{opp/same}$, is measured. $R_{opp/same}$ is shown as a function of the candidate p_T and compared with theory from [?] in Figure 5.3. As the p_T of the candidates increases beyond 0.3 GeV in Fig. 5.3, a transition from J/ψ that are uncorrelated with neutron production to J/ψ candidates that tend to be created in the same direction as the detected neutron.

The transition shown in Fig. 5.3 can be explained by the different neutron production processes that occur in coherent versus incoherent photoproduction [?]. In coherent photoproduction, the photon couples elastically to the nucleus as a whole. In this case the nucleus will typically stay ~~in-tacked~~intact. Neutron emission then occurs through exchange of an additional photon. The target struck by this additional photon need not be the same nucleus that was the target of the photoproduction process. For this reason, the neutron and J/ψ in coherent production are not expected to be correlated. Neutron emission in incoherent production is due to the excitation of the nucleus that occurs when the photon couples to ~~the~~an individual nucleon within the nucleus. The excited nucleus then decays by neutron emission. In this case, the target nucleus for both the J/ψ and the neutron are the same, and therefore correlated.

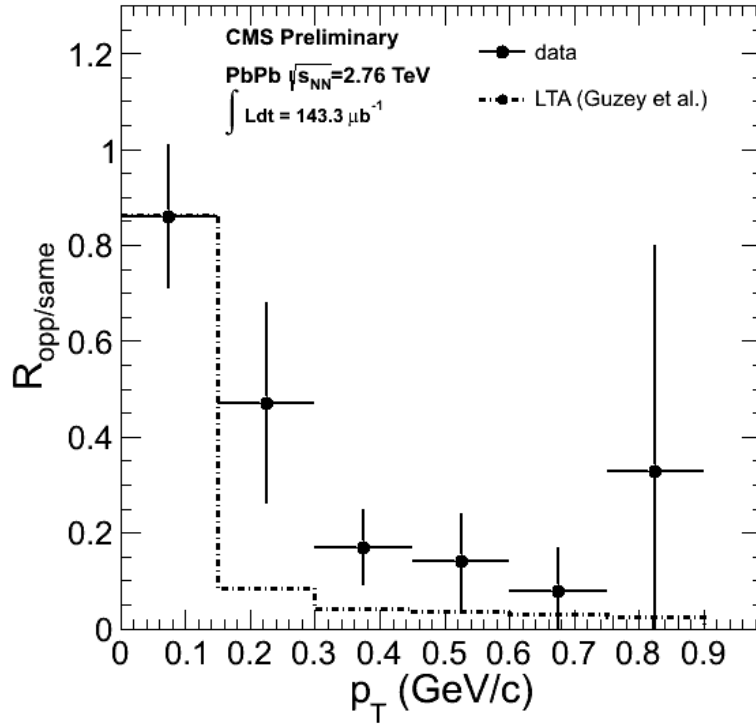


Figure 5.3: Ratio between the transverse momentum distribution of the J/ψ when J/ψ and neutron have the opposite direction and the transverse momentum distribution of the J/ψ when J/ψ and neutron have the same direction.

The correlation demonstrated in Fig. 5.3 can ~~potential~~potentially offer a means of separating the ~~part~~two terms of Eq.??, which probe different values of x . In incoherent events, because the neutron indicates the direction in which the target was traveling, the momentum of the photon can be deduced. If the photon carries higher longitudinal momentum than the gluons with which it interacts, the photoproduced J/ψ will be pushed by the photon in the direction opposite the emitted neutron. This would correspond to the low- x contribution to Eq.?. When the gluons within the nucleus are of higher longitudinal momentum, the J/ψ will travel in the direction of the target ~~and~~ ~~therefore~~and the emitted neutron~~giving~~. This gives the high- x contribution.

The measurement of $R_{opp/same}$ shown in Fig. 5.3 agrees qualitatively with the predictions of [?]. This indicates that neutron tagging can both aid in separating the coherent from the incoherent process, and potentially separate the low- x and high- x contribution to UPC photoproduction cross

sections at high rapidity values. However, this qualitative agreement requires additional theoretical and experimental work for quantitative confirmation.

5.3 Summary

As physicists' understanding of the QGP has deepened over the past 30 years of doing experimental heavy ion physics, the questions surrounding the QGP have shift from the confirmation of creation of a deconfined state to understanding the properties of the state that is created. It appears that the QGP is a hot nearly viscosity free fluid of strongly coupled quarks and gluons. The control measurements from dAu collisions at RHIC, and pPb collisions at the LHC have shown signs of collective behavior such as flow, which made these results difficult to interpret. Additional knowledge of the initial state of the colliding nuclei is needed in order to fully understand the QGP signal seen in PbPb and AuAu collisions. UPC events can provide this needed knowledge. This thesis contributes to the understanding of the initial state through the measurement of the UPC J/ψ photoproduction cross section.

Ultra-peripheral collisions are clean probe of the initial state. In UPC J/ψ photoproduction, the nuclei interact through the electromagnetic force precluding the possibility of creating a collective medium. The theoretical models of coherent UPC J/ψ photoproduction model these electromagnetic interactions by combining a semi-classical calculation of the photon flux with a variety of phenomenological and QCD based calculations of the nuclear gluon density. The Weisäcker-Williams approximation [?] is used to calculate the flux of photons that surround the colliding nuclei. The interaction of these photons with the nucleus is either calculated through a nuclear modification of the proton gluon density [?, ?], or by using the Glauber model approach that consists in modeling the nucleus as a collection of nucleons and scaling the nucleon photoproduction cross sections from e-p collisions [?]. Photoproduction cross sections from from UPC events can determine at what energy scale the Glauber based method breaks down. For the gluon density based calculations, there is a wide discrepancy between the predictions, and photoproduction cross

sections constrain which gluon density models are viable.

~~In this thesis, the CMS detector was used to measure the coherent UPC photoproduction cross section. The three major subsystems of CMS were used, the tracker, the muon system, the calorimeter system. The tracker records the position charge excitations in the silicon due to particle hits, which are used to reconstruct the trajectory of charged particles. The muon system is comprised of the three gaseous detectors, the DTs, the RPC, and the CSCs, which record charge deposits as high momentum particles ionize the gas within the detector. The muon system primary purpose is for triggering on and identifying muons. The calorimeter system measures the energy of deposited by particle induced showers as a means of reconstructing neutral particles and jets.~~

The analysis in this thesis consists of three major components, development of a trigger, estimation of efficiency, and measurement of signal events. The trigger development involved designing a trigger based on rate estimates from past data that ensured a sample that could be used for both measuring the signal and estimate the efficiency of the trigger, reconstruction, and event selection. The number of J/ψ candidates was measured by first applying a set of event selection cuts that rejected background events such as hadronic collisions and beam gas collisions, then fitting the remaining events to templates from simulation to separate the three remaining physics processes, the coherent, incoherent, and photon-photon process. The efficiencies for each part of the trigger were measured from data. The acceptance and reconstruction efficiency were estimated from MC. The cross section was calculated by combining the efficiency with the measured luminosity and number of coherent J/ψ . The statistical uncertainties were taken from the template fit. The systematic uncertainties were estimated by varying the method used on each component of the analysis.

The UPC J/ψ photoproduction cross section in the Xn0n break-up mode, $\frac{d\sigma_{co}^{J/\psi}}{dy}$ (Xn0n), was found to be ~~$368 \pm 38 \mu\text{b}$~~ 356 ± 71 (stat) $^{+43}_{-50}$ (syst) μb . When rescaled by a factor of 5.06 to account for the difference of break-up mode between the measurement in this thesis and the ALICE result in [?, ?], the result of ~~$1.86 \pm 19 \text{ mb}$~~ 1.80 ± 0.37 (stat) $^{+0.22}_{-0.25}$ (syst) mb was found to be consistent with the predictions in [?] ~~of 1.8 mb~~ . The calculation in [?] is also favored by the ALICE measurements. Of the gluon distributions used in [?], a gluon distribution with moderately strong

gluon shadowing, EPS09 [?], is consistent with both the results from this thesis and the previous ALICE results. This indicates that at the scale of the mass of the J/ψ the nucleus gluon density is significantly suppressed compared to the gluon densities of a nucleon. At this scale the nucleus can not be represented as a collection of nucleons as in the Glauber like model described in [?]. In addition, the J/ψ -neutron rapidity correlation shown in Fig. 5.3 by the $R_{\text{opp/same}}$ ratio demonstrates the potential to separate the low- x and high- x contributions to the photoproduction cross section.

The measurement in this thesis confirms the ability to increase the knowledge of the initial state through the exploration of UPC events. This confirmation opens the door to additional measurements in this growing field of UPC research. A whole host of measurements will be possible with the data already recorded, and with that to be recorded in the coming years by CMS and the other LHC experiments.